

1 This version of the article is a preprint; it was submitted on August 2, 2024 and has not been
2 peer reviewed. License: Creative Commons Attribution 4.0 International License.

3 **Number of words** (excluding acknowledgements and references): 8930

6 **Uncertainty-aware surrogate modeling for urban air** 7 **pollutant dispersion prediction**

8 Elliott Lumet^{1,2} · Mélanie C. Rochoux² · Thomas Jaravel² · Simon Lacroix³

9 **Abstract** This study evaluates a surrogate modeling approach that provides rapid en-
10 semble predictions of air pollutant dispersion in urban environments for varying meteorolo-
11 gical forcing, while estimating irreducible and modeling uncertainties. The POD–GPR
12 approach combining Proper Orthogonal Decomposition (POD) and Gaussian Process Re-
13 gression (GPR) is applied to emulate the response surface of a Large-Eddy Simulation
14 (LES) model of the Mock Urban Setting Test (MUST) field-scale experiment. We de-
15 sign and validate new methods for i) selecting the POD-latent space dimension to avoid
16 overfitting noisy structures due to atmospheric internal variability, and ii) estimating the
17 uncertainty in POD–GPR predictions. To train and validate the POD–GPR surrogate
18 in an offline phase, we build a large dataset of 200 LES 3-D time-averaged concentration
19 fields, which are subject to substantial spatial variability from near-source to background
20 concentration and have a very large dimension of several million grid cells. The results
21 show that POD–GPR reaches the best achievable accuracy levels, except for the highest
22 concentration near the source, while predicting full fields at a computational cost five
23 orders of magnitude lower than an LES. The results also show that the proposed mode
24 selection criterion avoids perturbing the surrogate response surface, and that the uncer-

¹Corresponding author: elliott.lumet@gmail.com

²CECI, Université de Toulouse, CNRS, CERFACS, 42 Avenue Gaspard Coriolis, 31057 Toulouse cedex 1, France

³LAAS-CNRS, Université de Toulouse, CNRS, 7 Avenue du Colonel Roche, BP54200, 31031 Toulouse cedex 4, France

25 tainty estimate explains a large part of the surrogate error and is spatially consistent with
26 the observed internal variability. Finally, POD–GPR can be robustly trained with much
27 smaller datasets, paving the way for application to realistic urban configurations.

28 **Keywords** Surrogate modeling · Uncertainty quantification · Microscale pollutant dis-
29 persion · Urban flow · Large-eddy simulation · Internal variability

30 1 Introduction

31 Accidental releases of pollutants into the atmosphere, such as from industrial accidents,
32 can degrade air quality and have significant short- and long-term health impacts (EEA
33 2020; Manisalidis et al. 2020). In urban environments, these risks are exacerbated by
34 high population density and reduced ventilation due to the urban canopy, leading to local
35 pollution peaks (Fernando et al. 2001; Klein et al. 2007; Pasquier et al. 2023). For accurate
36 mapping of these peaks and associated exposures, it is necessary to develop microscale
37 dispersion models that take into account i) the effect of urban buildings on the local flow,
38 and ii) the inherently multiscale and turbulent nature of the Atmospheric Boundary Layer
39 (ABL).

40 To gain relevant insight into these processes, there is a growing consensus in the re-
41 search community for the use of Computational Fluid Dynamics (CFD) (Blocken 2015;
42 Tominaga et al. 2023). Advanced models based on Reynolds-Averaged Navier-Stokes
43 (RANS) and Large-Eddy Simulation (LES) are able to represent complex flow structures,
44 in particular due to the interactions between the atmosphere and the built environment.
45 However, their use in operational applications remains limited because their high com-
46 putational cost prevents them from being used in real time, for example in emergency
47 response. Moreover, they still suffer from a lack of accuracy compared to field and wind
48 tunnel measurements due to the large uncertainties involved (Schatzmann and Leitl 2011;
49 Blocken 2014; Dauxois et al. 2021). These uncertainties can be classified into three dif-
50 ferent groups:

- 51 ○ *boundary condition uncertainties* due to measurement and representativeness errors

52 in calibration data, and to boundary condition modeling assumptions, in relation
53 to: i) the meteorological forcing (García-Sánchez et al. 2014; Lucas et al. 2016; Wise
54 et al. 2018), ii) the urban geometry representation (Santiago et al. 2010; Montazeri
55 and Blocken 2013; Gromke et al. 2016), and iii) the pollutant source (Winiarek et al.
56 2012; Spicer and Tickle 2021);

57 ◦ *structural modeling uncertainties*, inherent to the model solver and its underly-
58 ing modeling assumptions, mainly related to turbulence modeling (Tominaga and
59 Stathopoulos 2007; Blocken et al. 2008; Yue Yang and Wang 2008; Tominaga and
60 Stathopoulos 2009; Gorlé and Iaccarino 2013; Gorlé et al. 2015; Xiao et al. 2016);

61 ◦ *aleatory uncertainties*, mostly due to the turbulent and therefore stochastic nature
62 of the ABL, and referred to as internal variability, which results in an irreducible
63 uncertainty and is largely responsible for the discrepancies between field measure-
64 ments and CFD model predictions (Schatzmann and Leitl 2011; Neophytou et al.
65 2011; Antonioni et al. 2012; García-Sánchez et al. 2018; Dauxois et al. 2021; Lumet
66 et al. 2024b).

67 In this work, we focus on atmospheric uncertainties, i.e. in how to represent the impact
68 of large-scale atmospheric forcing uncertainties and internal variability on microscale LES
69 field predictions. We have chosen not to consider structural modeling uncertainties, as
70 these have been extensively studied and remain small in the LES context. Instead, we have
71 chosen to investigate how to design a surrogate modeling approach to quantify boundary
72 condition uncertainties in LES, while accounting for internal variability. To our knowledge,
73 the coupling between these two sources of uncertainty has not yet been studied, while this
74 is one challenge expressed by Dauxois et al. (2021) and Wu and Quan (2024).

75 Surrogate modeling, also known as reduced-order modeling, aims at accurately emulat-
76 ing the response surface of complex and expensive numerical models, while significantly
77 reducing computational time. By enabling real-time and large ensemble predictions, sur-
78rogate modeling is well suited to address the dual challenges of high cost and uncertainty
79 in LES models, making it a hot topic of research in the CFD field (Lassila et al. 2014;
80 Vinuesa and Brunton 2022). For parametric studies, surrogate models are mostly based

81 on fully data-driven approaches, which consist of learning the response surface of the
82 CFD model from a dataset of reference simulations precomputed during an offline phase,
83 to then provide fast predictions during an online phase. They have been successfully used
84 to emulate urban wind and/or pollutant dispersion, with respect to urban geometry (Wu
85 et al. 2021; Huang et al. 2022; Mendil et al. 2022; Kastner and Dogan 2023), or mete-
86 orological forcing and pollutant source (Margheri and Sagaut 2016; Xiang et al. 2021;
87 Nony et al. 2023). Surrogate models are therefore valuable for ensemble prediction in
88 more complex frameworks such as urban design optimization (Wu et al. 2021; Wu and
89 Quan 2024), sensitivity analysis (Cheng et al. 2020; Fellmann et al. 2023), uncertainty
90 quantification (García-Sánchez et al. 2014, 2017), and data assimilation (Mons et al. 2017;
91 Sousa et al. 2018; Sousa and Gorlé 2019; Lumet 2024).

92 While surrogate models have proven to be valuable tools for dealing with uncertainties
93 related to CFD model boundary conditions, few studies have addressed the representation
94 of internal variability, which is at least as important (Neophytou et al. 2011; Antonioni
95 et al. 2012; Lumet et al. 2024b). Moreover, surrogate models introduce a new form of
96 structural uncertainty: the model reduction error, i.e. the error of the surrogate model
97 relative to the full-order model. Our aim is to evaluate the model reduction error in a
98 comprehensive and robust way, and to assess the ability of the surrogate model to retrieve
99 reliable information on internal variability from the LES dataset and compare it with the
100 model reduction error.

101 To this end, we adopt a surrogate modeling approach called POD–GPR (Marrel et al.
102 2015), which combines Proper Orthogonal Decomposition (Sirovich 1987; Berkooz et al.
103 1993) and Gaussian Process Regression (Rasmussen et al. 2006). It is a robust and stan-
104 dard method that has already been used for urban wind and pollutant dispersion predic-
105 tion (Xiao et al. 2019; Xiang et al. 2021; Weerasuriya et al. 2021; Masoumi-Verki et al.
106 2022; Nony et al. 2023; Fellmann et al. 2023). In this study, we construct a POD–GPR
107 model for the MUST experiment of propylene dispersion in a simplified urban canopy
108 (Yee and Biltoft 2004). For this purpose, we generate a large dataset of 200 LES using
109 the model validated by Lumet et al. (2024b) by varying the wind boundary forcing. We

110 choose LES over the more common and less expensive RANS approach because: i) LES
111 is expected to reduce structural uncertainties due to turbulence modeling compared to
112 RANS (Gousseau et al. 2011; García-Sánchez et al. 2018), and ii) LES provides instantane-
113 ous snapshots of the most energetic atmospheric eddies and can thus be used to estimate
114 the effect of the microscale internal variability of the ABL on tracer dispersion (Lumet
115 et al. 2024b), which is central to the objective of this study.

116 The novelty of the proposed surrogate modeling approach is related to the POD latent
117 space, i.e. the reduced space compressing the LES information, and is twofold. First,
118 we define a method to choose a priori the POD-latent space dimension, based on the
119 projection of the internal variability into the latent space. Secondly, knowing the internal
120 variability in the LES data and using regression uncertainty estimates from Gaussian pro-
121 cesses, we develop a mathematical framework for propagating these uncertainty estimates
122 from the POD latent space to the physical space to help interpret the uncertainty results,
123 which to our knowledge has been little studied in physical applications.

124 This article is structured as follows: Section 2 briefly introduces the learning dataset
125 of LES simulations. Section 3 describes the POD–GPR surrogate modeling approach and
126 introduces our methods to estimate prediction uncertainty and select the latent space
127 dimension. Finally, Section 4 provides a comprehensive validation of the POD–GPR
128 predictions, uncertainty estimates, and ability to handle reduced-size training datasets.

129 **2 Learning dataset of large-eddy simulations**

130 This section summarizes the key points of the LES model for the MUST experiment,
131 which has been extensively validated in previous work (Lumet et al. 2024b) and which is
132 used here to build the surrogate learning dataset. Details are given on the choice of the
133 parameter space, the field quantities of interest and the associated internal variability.

134 **2.1 The MUST field campaign**

135 MUST is a field-scale experiment conducted in September 2001 at the US Army Dug-
136 way Proving Ground test site in Utah’s desert to collect extensive measurements of urban

137 pollutant dispersion (Biltoft 2001; Yee and Biltoft 2004). During the field campaign, a se-
138 ries of trials were carried out by releasing a passive tracer, propylene, at different locations
139 within an urban-like canopy consisting of 120 regularly-spaced shipping containers. It is
140 a canonical experiment for dispersion model validation: i) it was selected as one of the
141 reference case studies for the COST Action 732 CFD dispersion model intercomparison
142 (Franke et al. 2007), and ii) it has been used in a large number of CFD studies involving
143 RANS (Hanna et al. 2004; Hsieh et al. 2007; Milliez and Carissimo 2007; Donnelly et al.
144 2009; Efthimiou et al. 2011; Kumar et al. 2015; Bahlali et al. 2019) or LES (Camelli et al.
145 2005; Antonioni et al. 2012; König 2014; Nagel et al. 2022). In this study, we focus on
146 the trial 2681829 corresponding to neutral atmospheric conditions.

147 **2.2 LES model of the MUST field experiment**

148 We use the AVBP¹ (Schönfeld and Rudgyard 1999; Gicquel et al. 2011) code to
149 build the LES model. AVBP solves the LES-filtered Navier-Stokes equations on un-
150 structured mesh using a second-order Lax-Wendroff finite-volume centered numerical
151 scheme (Schönfeld and Rudgyard 1999) and using pressure gradient scaling since the
152 atmospheric flow features a low Mach number (Ramshaw et al. 1986). Tracer disper-
153 sion is modeled by the LES-filtered advection-diffusion equation using an Eulerian ap-
154 proach. Subgrid-scale turbulence is modeled using the Wall-Adaptative Local Eddy-
155 Viscosity (WALE) model (Nicoud and Ducros 1999) for subgrid momentum transport, and
156 a gradient-diffusion hypothesis for subgrid tracer transport (with the turbulent Schmidt
157 number equal to $S_c^t = 0.6$).

158 The computational domain is a rectangular box with dimensions of 420 m by 420 m by
159 50 m, discretized with a boundary-fitted mesh of 91 million tetrahedra, with a resolution
160 ranging from 0.3 m in the canopy to 5 m at the top of the domain.

161 In terms of boundary conditions, a logarithmic wind profile is imposed at the inlet so

¹AVBP documentation, see <https://www.cerfacs.fr/avbp7x/>

162 that the mean inlet wind velocity vector $\bar{\mathbf{u}}$ reads

$$\bar{\mathbf{u}} = \begin{pmatrix} \overline{u_{inlet}} \cos(\alpha_{inlet}) \\ \overline{u_{inlet}} \sin(\alpha_{inlet}) \\ 0 \end{pmatrix}, \quad \text{with } \overline{u_{inlet}}(z) = \frac{u_*}{\kappa} \ln \left(\frac{z + z_0}{z_0} \right), \quad (1)$$

163 where κ is the von Kármán constant equal to 0.4, z_0 is the aerodynamic roughness length,
 164 and u_* is the friction velocity. In addition, a synthetic turbulence injection method
 165 (Kraichnan 1970; Smirnov et al. 2001) is used to impose the upstream wind fluctua-
 166 tions based on a precomputed Reynolds tensor from a precursor run (corresponding to
 167 a simulation with the same surface roughness but without obstacles, and with periodic
 168 boundary conditions at the inlet and outlet inspired by Vasaturo et al. (2018)). At the
 169 lateral boundaries, symmetry boundary conditions are used. Static pressure is imposed
 170 at the outlet and top boundaries. Standard laws of the wall are imposed for the ground
 171 and obstacle boundaries. The pollutant source is modeled by a local source term in the
 172 advection-diffusion equation to match the experimental volumetric flow rate. A more
 173 detailed description of the boundary conditions is given in Lumet et al. (2024b).

174 To be comparable to the MUST observational time series, we need to simulate a 200-
 175 s time sequence for each snapshot of the learning dataset. Before running this time
 176 sequence, we need to initialize each simulation until first- and second-order statistics of
 177 the flow and tracer variables reach a stationary state. For this initialization, a spin-up
 178 time $t_{spin-up}$ of 1.5 times the convective time scale is used:

$$t_{spin-up} = 1.5 \times \left(\frac{L}{U_{bulk}} \right) = 1.5 \times \frac{\kappa H L}{u_* \left[(H + z_0) \ln \left(\frac{H+z_0}{z_0} \right) - H \right]}, \quad (2)$$

179 with $L = 420$ m the domain length and $H = 50$ m the domain height. This spin-up
 180 time is specific to each snapshot as the bulk velocity U_{bulk} is an uncertain quantity
 181 (Sect. 2.3). Note that the average computational cost for a given simulation of 200 s
 182 is around 15,000 core hours, which motivates the development of a surrogate model to
 183 speed up predictions.

184 **2.3 Definition of the input parameter space**

185 **2.3.1 Choice of input parameters**

186 In this work, we focus on atmospheric parametric uncertainties. For the surrogate
187 model to be useful, it must capture the dependence of the tracer dispersion on the most
188 influential and uncertain atmospheric parameters of the LES model. In preliminary work
189 (Lumet (2024), Chapter III), we carried out one-at-a-time sensitivity analysis and showed
190 that the inlet wind direction α_{inlet} and the friction velocity u_* are the two parameters
191 that most significantly affect the LES mean concentration predictions. In particular, the
192 aerodynamic roughness length z_0 is well identified in the MUST experiment (z_0 is equal
193 to 0.045 ± 0.005 m according to observations, Yee and Biltoft (2004)) and was found to
194 have a negligible impact. For these reasons, we consider only two uncertain parameters:

$$\boldsymbol{\theta} = (\alpha_{inlet}, u_*), \quad (3)$$

195 to define the input space of the surrogate model. Note that this choice is quite common
196 in urban flow surrogate modeling (Margheri and Sagaut 2016; García-Sánchez et al. 2014,
197 2017). Note also that, under neutral conditions, the mean concentration is inversely
198 proportional to the friction velocity and the reduction problem could thus be simplified
199 by predicting dimensionless quantities, as done by Sousa et al. (2018) and Lamberti and
200 Gorlé (2021). This normalization was investigated in Lumet (2024), Chapter IV, but we
201 choose to present results with multiple input dimensions here for generalization purposes.

202 **2.3.2 Parameter variation ranges**

203 The surrogate model must cover a wide, but plausible and feasible, range of variation
204 in the input parameters (Eq. 3). Based on a microclimatology constructed using all
205 available data from the closest micrometeorological station to the MUST site (Lumet
206 (2024), Chapter IV), all wind directions are likely to occur and more than 99% of the
207 horizontal wind speed measurements at $z = 10$ m are below 12 m s^{-1} , which corresponds
208 to a friction velocity u_* of 0.89 m s^{-1} and which is therefore chosen as the maximum friction

209 velocity here. We limit the minimum friction velocity to 0.07 m s^{-1} , which corresponds
 210 to a wind speed of about 1 m s^{-1} at an altitude of 10 m, since we are interested in windy
 211 conditions. To reduce the number of LES, we also restrict the range of variation for the
 212 inlet wind direction to wind directions for which the plume crosses the array of containers.
 213 In the end, the input parameter space reads

$$\Omega_{\theta} = [-90^{\circ}, 30^{\circ}] \times [0.07 \text{ m s}^{-1}, 0.89 \text{ m s}^{-1}]. \quad (4)$$

214 2.3.3 Parameter space sampling

215 To sample the input parameter space (Eq. 4), we use Halton's sequence (1964). As
 216 a low-discrepancy sequence, it samples the space uniformly and more efficiently than a
 217 purely random sequence for a limited number of samples, avoiding redundant sampling
 218 in the same areas and it is well adapted to a small number of parameters. Figure 1 shows
 219 the location of the 200 samples thus obtained in the uncertain parameter space.

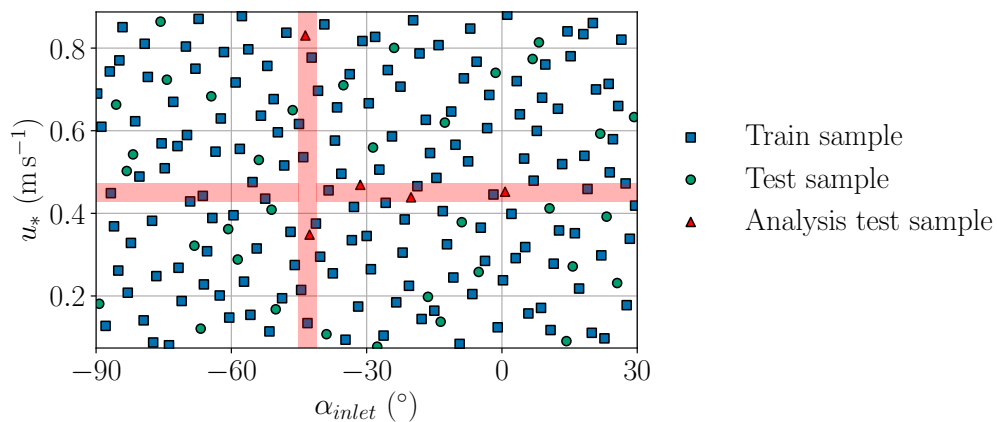


Figure 1: *Input parameter space sampling obtained with Halton's sequence. Each point is a pair of parameters for which we perform an LES prediction. The training (80%) and test (20%) sets are represented as blue squares and green circles, respectively. The horizontal red shaded area corresponds to the parameter space sub-section scanned by taking a margin of $\pm 5\%$ around the constant friction speed $u_*^{\text{plot}} = 0.45 \text{ m s}^{-1}$. The vertical shaded area is similarly defined around the constant inlet wind direction $\alpha_{\text{inlet}}^{\text{plot}} = -43^{\circ}$ with a margin of $\pm 2^{\circ}$. The test samples within these ranges (red triangles) are used in Sect. 4.3 to evaluate the surrogate model.*

220 **2.4 Generation of the LES dataset**

221 We run an LES for each of the 200 input parameter samples (Fig. 1) to provide the
222 learning dataset for the surrogate model. The main quantity of interest for the surrogate
223 modeling approach is the 3-D mean (time-averaged) concentration field averaged over the
224 200-s analysis time period of the MUST experiment.

225 To generate this ensemble, the computational domain is rotated to align with the mean
226 wind direction α_{inlet} to avoid inducing lateral confinement and numerical instabilities due
227 to the shear-free boundary conditions at the domain sides. The spin-up time before
228 collecting LES statistics is scaled by the friction velocity according to Eq. 2 to account
229 for the slowing down of the flow establishment with decreasing u_* . Finally, the Reynolds
230 stress tensor prescribed for the turbulent injection method is rescaled by u_*^2 following
231 similarity theory.

232 The total cost of generating this LES ensemble is about 5.7 million core hours. Note
233 that a subset of the most relevant data from these simulations, including all the data used
234 in this study, is available in open access (Lumet et al. 2024a).

235 Figure 2a shows the topology of the LES ensemble with the example of the mean
236 concentration c at one specific location within the canopy (the green square in Fig. 2b,
237 c corresponding to the tower B in the MUST experiment). The mean concentration
238 increases linearly with decreasing friction velocity. The dependence on the wind direction
239 is more complex with a concentration maximum obtained for $\alpha_{inlet} \approx 30^\circ$ and a rapid
240 decay in both directions down to 0 ppm as the plume no longer crosses the probe location.
241 The two examples of horizontal cuts of the LES mean concentration fields (Fig. 2b, c)
242 obtained for two different wind conditions highlight the high spatial variability of the fields,
243 especially within the plumes, which is a challenge for the surrogate modeling problem.

244 **2.5 Noise in the learning dataset**

245 Atmospheric flows are naturally unsteady with strong variations occurring over a wide
246 range of frequencies corresponding to the time scales of the atmospheric eddies. When
247 considering statistics over finite temporal periods, this internal variability yields sampling

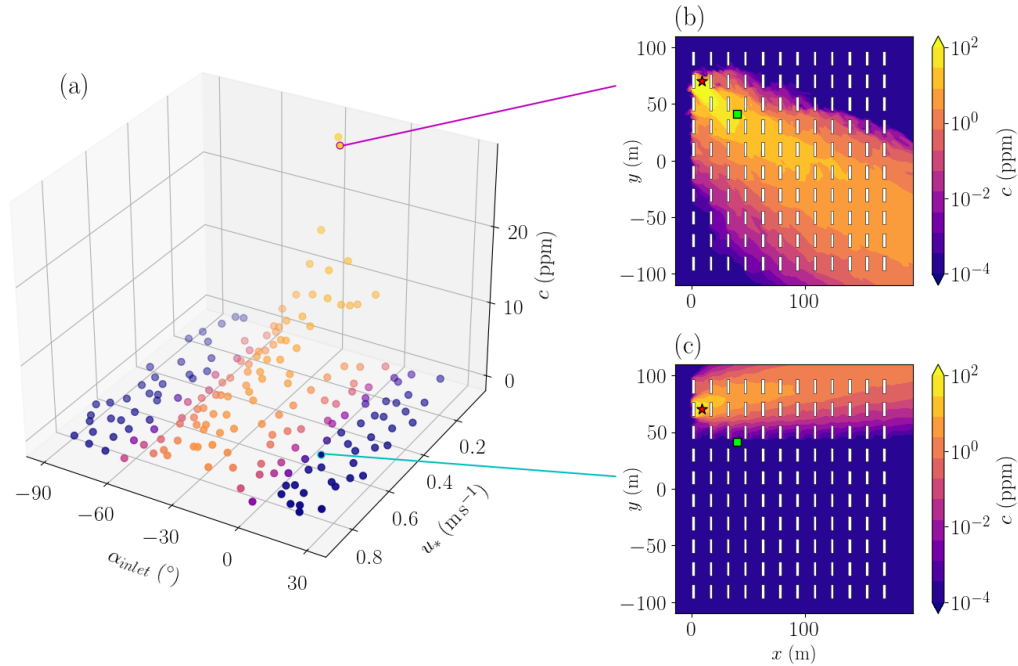


Figure 2: (a) LES prediction of the local mean (time-averaged) concentration c at tower B at $z = 2$ m for each sample of parameters $\theta = (\alpha_{inlet}, u_*)$ from Fig. 1. (b, c) Horizontal cuts of the mean concentration at $z = 1.6$ m for the two samples $(\alpha_{inlet}^{(81)}, u_*^{(81)}) = (-27.7^\circ, 0.08 \text{ m s}^{-1})$ and $(\alpha_{inlet}^{(133)}, u_*^{(133)}) = (7.73^\circ, 0.60 \text{ m s}^{-1})$ in (a). The green square corresponds to the tower B, and the red star corresponds to the tracer source.

248 errors and is therefore a source of aleatory uncertainty, which is inherent to the physical
 249 system under study and thereby irreducible. For the MUST case, internal variability has a
 250 significant impact on the tracer concentration statistics when computed over the standard
 251 200-s analysis period (Schatzmann et al. 2010; Lumet et al. 2024b). One of the challenges
 252 of this study is to build a surrogate model that explicitly estimates this uncertainty when
 253 emulating the mean concentration fields.

254 To quantify the effect of internal variability on the LES predictions, we use the sta-
 255 tionary bootstrap approach from Lumet et al. (2024b), which relies on resampling of the
 256 sub-averages of the physical fields using the algorithm of Politis and Romano (1994) and
 257 which involves a mean bootstrap block length to account for temporal correlation between
 258 sub-averages. This approach is applied separately for each snapshot in the dataset (Fig. 1)
 259 using 1,000 bootstrap replicates to estimate the internal variability.

260 Figure 3 confirms that the internal microscale variability of the ABL significantly

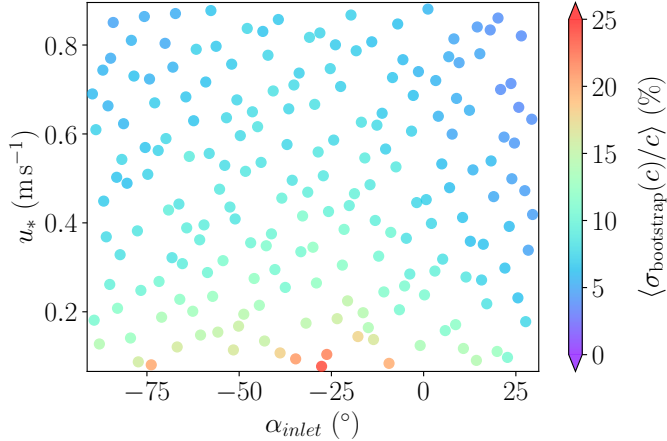


Figure 3: Relative uncertainty of the mean concentration in the parameter space estimated using stationary bootstrap (Lumet et al. 2024b) and averaged over the whole spatial domain. Each circle corresponds to the averaged uncertainty of one LES sample of the learning dataset obtained from Halton’s sequence (Fig. 1).

261 affects the LES learning dataset, with spatially-averaged relative standard deviations
 262 of up to just over 20% for a few samples of the LES dataset. Looking at the mean
 263 concentration fields, these deviations can be even larger locally, especially in areas of
 264 strong gradients or close to the source. We note in Fig. 3 that the noise induced by
 265 internal variability is not homogeneous in the input parameter space, as it increases as
 266 the friction velocity decreases. This is because as advection decreases, the temporal
 267 correlation of concentration increases, which increases the uncertainty of the mean over
 268 the 200-s analysis period (less independent information to estimate the mean). We also
 269 note that the noise decreases as α_{inlet} moves away from the median value of -30° , due
 270 to a zoning bias: the plume moves further outside the domain at the boundary angles
 271 (Eq. 4), and there is therefore a larger proportion of the domain where the concentration
 272 is zero at these angles.

273 This quantification of the noise in the learning dataset is of paramount importance for
 274 the construction and validation of surrogate models. In particular, this information can
 275 be used to select the dimension of the latent space to prevent the surrogate model from
 276 overfitting the noise associated with internal variability (Sect. 3.4). Internal variability
 277 estimates can also be used as a reference to check that the surrogate model uncertainty
 278 is not underestimated (Sect. 3.3), and as a performance target for the surrogate model

279 (Sect. 3.5).

280 **3 Surrogate modeling approach**

281 This section presents the POD–GPR surrogate modeling approach and specifies the
282 inputs/outputs and metrics used for validation. The focus is on two points. The first point
283 is how to estimate the uncertainty associated with POD–GPR predictions and relate it
284 to internal variability. The second point is how to make an informed choice about the
285 surrogate latent space dimension.

286 **3.1 Problem statement**

287 The goal of the surrogate model is to emulate as closely as possible the response surface
288 of the LES model (Sect. 2.2) with respect to the input parameters $\boldsymbol{\theta} = (\alpha_{inlet}, u_*)$ defined
289 over the space $\Omega_{\boldsymbol{\theta}}$ (Eq. 4, Sect. 2.3). This means finding a function:

$$\begin{aligned} \mathcal{M}_{\text{surrogate}} : \Omega_{\boldsymbol{\theta}} &\longrightarrow \mathbb{R}^N, \\ \boldsymbol{\theta} &\longmapsto \mathbf{y}_{\text{surrogate}}, \end{aligned} \tag{5}$$

290 that minimizes $\int_{\Omega_{\boldsymbol{\theta}}} \|\mathbf{y}_{\text{surrogate}}(\boldsymbol{\theta}) - \mathbf{y}_{\text{LES}}(\boldsymbol{\theta})\| d\boldsymbol{\theta}$, where $\mathbf{y}_{\text{LES}} \in \mathbb{R}^N$ is the field to be
291 emulated, discretized on a grid of N nodes, and where $\mathbf{y}_{\text{surrogate}}$ is its counterpart predicted
292 by the surrogate. This function is obtained here by learning from the train dataset
293 $\left\{ \left(\boldsymbol{\theta}^{(i)}, \mathbf{y}_{\text{LES}}(\boldsymbol{\theta}^{(i)}) \right) \right\}_{i=1}^{N_{\text{train}}}$ with $N_{\text{train}} = 160$ (80% of the full LES dataset, see Fig. 1).

294 In this study, we focus on the emulation of the mean tracer concentration fields, which
295 are noisy due to the internal variability of the ABL (Sect. 2.5). Taking into account this
296 aleatory uncertainty in the construction and validation of the surrogate model is a key
297 challenge we address here.

298 To reduce the computational cost associated with the high dimension N of the solver
299 grid on which the fields of interest are expressed, we interpolate all the fields on an analysis
300 mesh twice as coarse, centered around the container array, and with a height limited to
301 20 m as most of the tracer is located in this area. This leads to an analysis mesh of

302 $N = 1.88 \times 10^6$ nodes, with characteristic cell sizes ranging from 0.6 m to 4 m, which
303 facilitates efficient model reduction. We have checked that using a coarser-resolution
304 mesh has a negligible effect on the surrogate model accuracy (not shown here).

305 **3.2 The POD–GPR surrogate model**

306 **3.2.1 Principle**

307 We choose to use a POD–GPR surrogate model because it has proven to be efficient,
308 relatively inexpensive and robust (Marrel et al. 2015; Guo and Hesthaven 2018; Nony
309 et al. 2023). The fundamental principle of the POD–GPR approach is to combine:

- 310 i) a *reduction step* using Proper Orthogonal Decomposition (POD) (Sirovich 1987;
311 Berkooz et al. 1993), which is very popular in fluid mechanics (Chinesta et al.
312 2011; Taira et al. 2017; Vinuesa and Brunton 2022) and consists in finding a low-
313 dimensional space, called *latent space*, of dimension $L \ll N$, on which the fields to
314 be emulated $\mathbf{y}(\boldsymbol{\theta})$ are projected;
- 315 ii) and a *regression step* using standard Gaussian Process Regression (GPR) (Ras-
316 mussen et al. 2006), which consists in learning from the train set, the relationship
317 between the LES model input parameters $\boldsymbol{\theta}$ and the latent coefficients $\{k_\ell(\boldsymbol{\theta})\}_{\ell=1}^L$
318 resulting from the field projection onto the latent space.

319 This reduction-regression approach allows i) to reduce the dimension of the regression
320 problem to L latent variables ($L \ll N$) and thereby drastically reduce the computational
321 burden of the learning task; and ii) to separate the parametric dependence of the field
322 from the spatial variability.

323 The POD–GPR model is implemented as a standard statistical learning approach,
324 i.e. with an initial training phase consisting of i) preprocessing the LES fields, ii) building
325 the POD reduced basis based on the train set, and iii) optimizing the GPR models in
326 the latent space (Fig. 4a). This training phase is done offline and only once. The trained
327 POD–GPR can then provide online field predictions for new inputs $\boldsymbol{\theta}$ as follows: i) the
328 associated POD reduced coefficients are predicted by the fitted GPR models, and ii) the

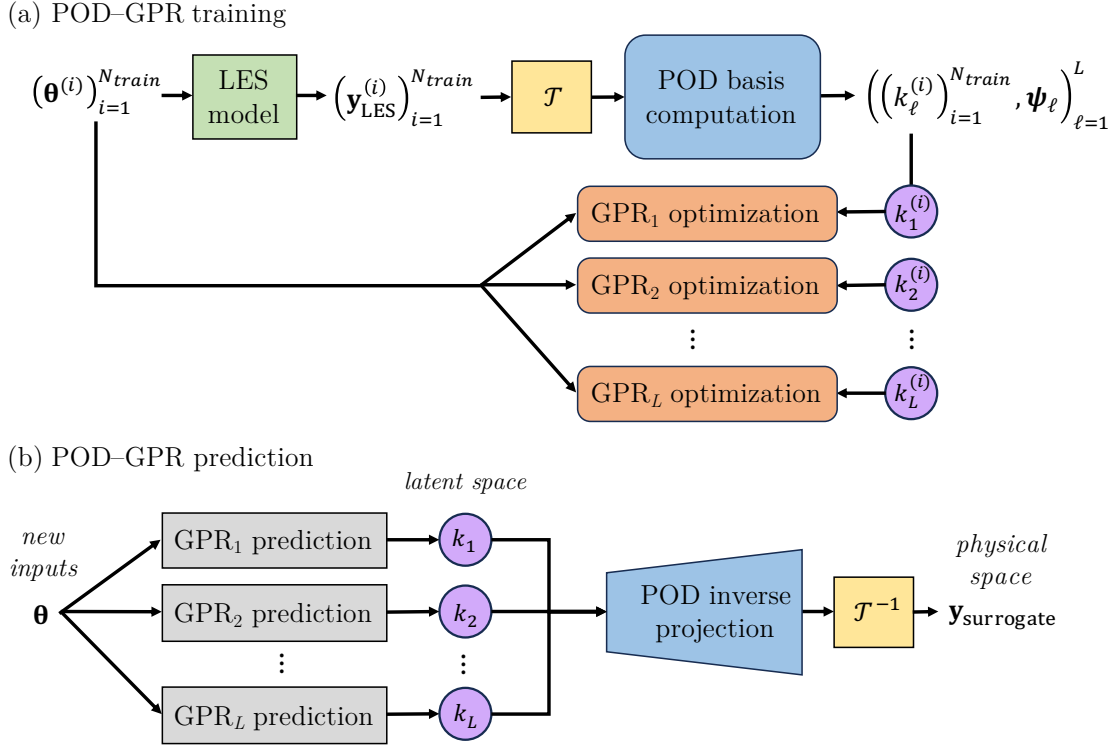


Figure 4: Schematic of the POD-GPR surrogate model. Its operation is divided into two stages: the training phase (a), and the prediction phase (b). For the training phase, first, a preprocessing \mathcal{T} is applied to the LES predicted fields, and the POD reduced basis (ψ_1, \dots, ψ_L) is built on the scaled train set; then L independent GPR models are optimized to emulate the L POD reduced coefficients (k_1, \dots, k_L) for the input parameters θ . For the prediction phase, the fitted GPR models predict the POD reduced coefficients associated with a given set of wind conditions θ , then the inverse POD projection and inverse scaling \mathcal{T}^{-1} are applied to recover the associated physical field.

329 inverse POD projection and inverse fields scaling are applied to these coefficients to re-
 330 cover the physical field $\mathbf{y}_{\text{surrogate}}$ (Fig. 4b). The following sections present the theoretical
 331 elements of the POD and GPR techniques required for this study.

332 3.2.2 Field preprocessing and dimension reduction using POD

333 With POD, the fields are projected linearly into the latent space generated by the
 334 L eigenvectors $\{\psi_\ell\}_{\ell=1}^L$ of the train set covariance matrix associated with the L largest
 335 eigenvalues $\{\Lambda_\ell\}_{\ell=1}^L$. These eigenvalues are the most informative about the coherent
 336 spatial structures emerging from variations in the wind conditions $\theta = (\alpha_{\text{inlet}}, u_*)$. The
 337 question of how to choose L is discussed further in Sect. 3.4.

338 The projection of one field $\mathcal{T}(\mathbf{y})$ onto the POD latent space can be formulated as

$$\mathcal{T}(\mathbf{y}) \approx \sum_{\ell=1}^L \sqrt{\Lambda_\ell} k_\ell \boldsymbol{\psi}_\ell, \quad (6)$$

339 where \mathcal{T} is a field preprocessing treatment including centering, and $\{k_\ell\}_{\ell=1}^L$ are the POD
 340 reduced coefficients defined as the coefficients in the projection of the given field $\mathbf{y}(\boldsymbol{\theta})$
 341 normalized by $\sqrt{\Lambda_\ell}$. This scaling, called POD whitening (Kessy et al. 2018), ensures that
 342 the set of reduced coefficients $\{k_\ell\}_{\ell=1}^L$ is centered and has unit component-wise variances
 343 on average, so that the regression problem is well posed for GPR.

344 The orthogonality of POD modes leads to some very useful properties (Berkooz et al.
 345 1993; Cordier and Bergmann 2006): i) the POD decomposition (Eq. 6) is the linear
 346 combination that reproduces the most variance of the original set, and ii) POD reduced
 347 coefficients are uncorrelated, i.e. $\text{Cov}(k_i, k_j) = 0$, if $i \neq j$, which justifies why we build
 348 one GPR model per mode (Fig. 4).

349 For pollutant dispersion applications, a particular difficulty arises from the wide dis-
 350 parity of the concentration scale, which significantly limits POD approximation accuracy.
 351 This can be addressed by preprocessing the fields before building the POD, as this changes
 352 the meaning of the optimality and orthogonality properties of the POD modes (Schmidt
 353 and Colonius 2020), and thus conditions the POD ability to efficiently represent fields
 354 in a smaller dimension. Using a logarithmic preprocessing, which is a natural choice for
 355 concentrations that decrease exponentially with distance from the source, results in better
 356 overall projection performance for the MUST case study (not shown here – see Lumet
 357 (2024), Chapter IV, for further discussion on preprocessing strategies). This logarithmic
 358 preprocessing reads:

$$\begin{aligned} \mathcal{T} : \mathbb{R}^N &\longrightarrow \mathbb{R}^N, \\ \mathbf{y}(\mathbf{x}_k) &\longmapsto \sqrt{\frac{\omega(\mathbf{x}_k)}{\Omega}} [\ln(\mathbf{y}(\mathbf{x}_k) + y_t) - \langle \ln(\mathbf{y}_{\text{LES}}(\mathbf{x}_k) + y_t) \rangle], \quad 1 \leq k \leq N, \end{aligned} \quad (7)$$

359 where $\frac{\omega(\mathbf{x}_k)}{\Omega}$ is the relative volume of the node \mathbf{x}_k , and y_t is a threshold set to 10^{-4} ppm

360 to avoid issues with concentration values close to zero. This choice provides an effective
 361 compromise that does not over-cut low concentrations and does not over-emphasize very
 362 low variances, which are mainly numerical noise. Note that this preprocessing also includes
 363 the centering required for POD (Berkooz et al. 1993), and volume node weighting to avoid
 364 over-weighting refined locations (Schmidt and Colonius 2020).

365 3.2.3 Latent coefficients estimation by Gaussian processes

366 Once the POD latent space is constructed, the next step is to predict the POD reduced
 367 coefficients $\{k_\ell(\boldsymbol{\theta})\}_{\ell=1}^L$ for any new wind conditions $\boldsymbol{\theta} \in \Omega_\theta$ (Fig. 4b). Since POD coeffi-
 368 cients are uncorrelated, we simplify this vector regression problem into L scalar regression
 369 problems solved by GPR (Rasmussen et al. 2006). There are three main reasons for this
 370 choice: i) simple interpolation may fail to predict latent space components (Brunton and
 371 Kutz 2019); ii) GPR was found to be one of the best machine learning regression meth-
 372 ods for predicting POD-reduced coefficients of LES concentration fields (Nony 2023); and
 373 iii) GPR models predict probability distributions and not just pointwise estimates, which
 374 is in line with our objective to quantify surrogate model uncertainties.

375 The principle of Gaussian processes (GP) is that the data distribution can be described
 376 by a Gaussian stochastic process, implying

$$k_\ell = f_\ell(\boldsymbol{\theta}) + \epsilon_\ell \text{ with } \begin{cases} f_\ell(\boldsymbol{\theta}) \sim \mathcal{GP}(\mathbf{0}, r_\ell(\boldsymbol{\theta}, \boldsymbol{\theta}^*)), \forall (\boldsymbol{\theta}, \boldsymbol{\theta}^*) \in \Omega_\theta^2 \\ \epsilon_\ell \sim \mathcal{N}(0, s_\ell^2) \end{cases}, \quad (8)$$

377 where r_ℓ is the GP covariance function, or *kernel*, and where ϵ_ℓ is an additive Gaussian
 378 noise with variance s_ℓ^2 accounting for the fact that the k_ℓ are subject to an irreducible noise
 379 due to the internal variability of the mean concentration (Fig. 3). Note that we assume
 380 that the prior distribution of the GP is zero on average since POD reduced coefficients
 381 are centered on average.

382 Given the property that any finite subset of realizations of a GP follows a multivariate
 383 Gaussian distribution, the posterior probability distribution of the quantity of interest

384 $k_\ell^*(\boldsymbol{\theta}^*)$ knowing the training set $\{\boldsymbol{\theta}^{train}, \mathbf{K}_\ell^{train}\}$ is

$$k_\ell^*(\boldsymbol{\theta}^*) \Big|_{\{\boldsymbol{\theta}^{train}, \mathbf{K}_\ell^{train}\}} \sim \mathcal{N}\left(\mu_\ell, \sigma_{\text{GP}}^2(k_\ell^*)\right), \quad (9)$$

385 with:

$$\begin{cases} \mu_\ell = r_\ell(\boldsymbol{\theta}^*, \boldsymbol{\theta}^{train}) \left[r_\ell(\boldsymbol{\theta}^{train}, \boldsymbol{\theta}^{train}) + s_\ell^2 \mathbf{I} \right]^{-1} \mathbf{K}_\ell^{train}, & (10a) \\ \sigma_{\text{GP}}^2(k_\ell^*) = r_\ell(\boldsymbol{\theta}^*, \boldsymbol{\theta}^*) + s_\ell^2 - r_\ell(\boldsymbol{\theta}^*, \boldsymbol{\theta}^{train}) \left[r_\ell(\boldsymbol{\theta}^{train}, \boldsymbol{\theta}^{train}) + s_\ell^2 \mathbf{I} \right]^{-1} r_\ell(\boldsymbol{\theta}^{train}, \boldsymbol{\theta}^*). & (10b) \end{cases}$$

386 In the regression context, these equations give the mean GPR prediction (Eq. 10a)
 387 and the associated variance (Eq. 10b), which quantifies two forms of uncertainty: i) the
 388 uncertainty linked to the noise in the training data and related to the term $s_\ell^2 \mathbf{I}$, and ii) the
 389 regression uncertainty that depends on the distance between the new input parameters
 390 $\boldsymbol{\theta}^*$ and the training parameters $\boldsymbol{\theta}^{train}$. Both equations involve the kernel r_ℓ , which is here
 391 of standard Matérn type with hyperparameter $\nu = 5/2$ (Stein 1999).

392 In the end, each GP has four hyperparameters: the noise variance s_ℓ^2 , and three pa-
 393 rameters involved in the Matérn kernel (Stein 1999): the maximum allowable covariance,
 394 and the length scale associated with each of the two uncertain parameters. These param-
 395 eters are determined by maximum log-likelihood estimation (Hastie et al. 2009) during
 396 GP optimization (Fig. 4a).

397 3.3 Uncertainty estimation of POD–GPR predictions

398 Below we explain how the GPR estimated uncertainty (Eq. 10b) is propagated from
 399 latent space to physical space through the POD inverse projection. This is useful to
 400 quantify the uncertainty of POD–GPR field predictions.

401 POD–GPR predictions are defined as linear combinations of the POD reduced coeffi-
 402 cients $k_\ell(\boldsymbol{\theta})$ (Eq. 6), which are uncorrelated (by POD modeling assumption) and normally
 403 distributed (Eq. 9). Consequently, at each grid node \mathbf{x}_k , the variance of the POD–GPR

404 prediction $\mathcal{T}(\mathbf{y}(\boldsymbol{\theta}, \mathbf{x}_k))$ also follows a normal distribution:

$$\sigma_{\text{POD-GPR}}^2(\mathcal{T}(\mathbf{y}(\boldsymbol{\theta}, \mathbf{x}_k))) = \sum_{\ell=1}^L \Lambda_{\ell} \sigma_{\text{GP}}^2(k_{\ell}(\boldsymbol{\theta})) \psi_{\ell}(\mathbf{x}_k)^2, \quad (11)$$

405 with $\sigma_{\text{GP}}^2(k_{\ell}(\boldsymbol{\theta}))$ the ℓ th GP variance (Eq. 10b).

406 Using log-preprocessing (Eq. 7), we deduce that the variance of the re-scaled mean
407 concentration prediction $\mathbf{y}(\boldsymbol{\theta}, \mathbf{x}_k)$ follows a log-normal distribution:

$$\sigma_{\text{POD-GPR}}^2(\mathbf{y}(\boldsymbol{\theta}, \mathbf{x}_k)) = \left[\exp(s(\boldsymbol{\theta}, \mathbf{x}_k)^2) - 1 \right] \times \exp(2m(\boldsymbol{\theta}, \mathbf{x}_k) + s(\boldsymbol{\theta}, \mathbf{x}_k)^2), \quad (12)$$

408 where:

$$\left\{ \begin{array}{l} m(\boldsymbol{\theta}, \mathbf{x}_k) = \sqrt{\frac{\Omega}{\omega(\mathbf{x}_k)}} \sum_{\ell=1}^L \sqrt{\Lambda_{\ell}} k_{\ell} \psi_{\ell}(\mathbf{x}_k) + \langle \ln(\mathbf{y}_{\text{LES}} + y_t) \rangle, \\ s(\boldsymbol{\theta}, \mathbf{x}_k)^2 = \left(\frac{\Omega}{\omega(\mathbf{x}_k)} \right) \sum_{\ell=1}^L \Lambda_{\ell} \sigma_{\text{GP}}^2(k_{\ell}(\boldsymbol{\theta})) \psi_{\ell}(\mathbf{x}_k)^2. \end{array} \right. \quad (13a)$$

$$\left\{ \begin{array}{l} m(\boldsymbol{\theta}, \mathbf{x}_k) = \sqrt{\frac{\Omega}{\omega(\mathbf{x}_k)}} \sum_{\ell=1}^L \sqrt{\Lambda_{\ell}} k_{\ell} \psi_{\ell}(\mathbf{x}_k) + \langle \ln(\mathbf{y}_{\text{LES}} + y_t) \rangle, \\ s(\boldsymbol{\theta}, \mathbf{x}_k)^2 = \left(\frac{\Omega}{\omega(\mathbf{x}_k)} \right) \sum_{\ell=1}^L \Lambda_{\ell} \sigma_{\text{GP}}^2(k_{\ell}(\boldsymbol{\theta})) \psi_{\ell}(\mathbf{x}_k)^2. \end{array} \right. \quad (13b)$$

409 Equation 12 provides an estimate of the uncertainty associated with POD-GPR predic-
410 tions. This uncertainty is the sum of the GP variances $\sigma_{\text{GP}}^2(k_{\ell}(\boldsymbol{\theta}))$, which quantify the
411 noise error in the training data and the regression error for each mode. In this context,
412 these two forms of error therefore correspond to the uncertainty associated with the LES
413 internal variability (Sect. 2.5) and to part of the structural error associated with model
414 reduction. It is worth noting that this estimate does not include the error associated with
415 the projection into the POD latent space.

416 3.4 A priori choice of latent space dimension

417 The choice of the POD latent space dimension is case-dependent and has a critical
418 effect on the accuracy of the surrogate model. On the one hand, the higher the number of
419 POD modes, the more variance of the original ensemble is captured in the POD reduced
420 basis. On the other hand, high-order modes are likely to encode noise in the train set
421 (Forkman et al. 2019), and are therefore best set aside to prevent GP from overfitting
422 noise during learning. In this section, we present an innovative method to select L as a

423 trade-off between the total variance embedded in the POD reduced basis and the amount
 424 of noise carried by the POD modes.

425 **POD projection error** First, we evaluate the POD projection error, i.e. the error ob-
 426 tained after reconstructing the fields projected onto the POD latent space through inverse
 427 POD transformation, for varying number of modes L following the approach adopted by
 428 Nony et al. (2023). Figure 5a shows that the POD projection normalized mean square
 429 error (NMSE) quickly decreases with the number of modes, and that a small number of
 430 modes ($L \approx 5-10$) allows to obtain very fine NMSE scores. We verify that the eigenvalues
 431 Λ_ℓ are a good proxy for quantifying the amount of information retrieved by each POD
 432 mode (Berkooz et al. 1993) and can therefore be used to select L as done by Xiao et al.
 (2019).

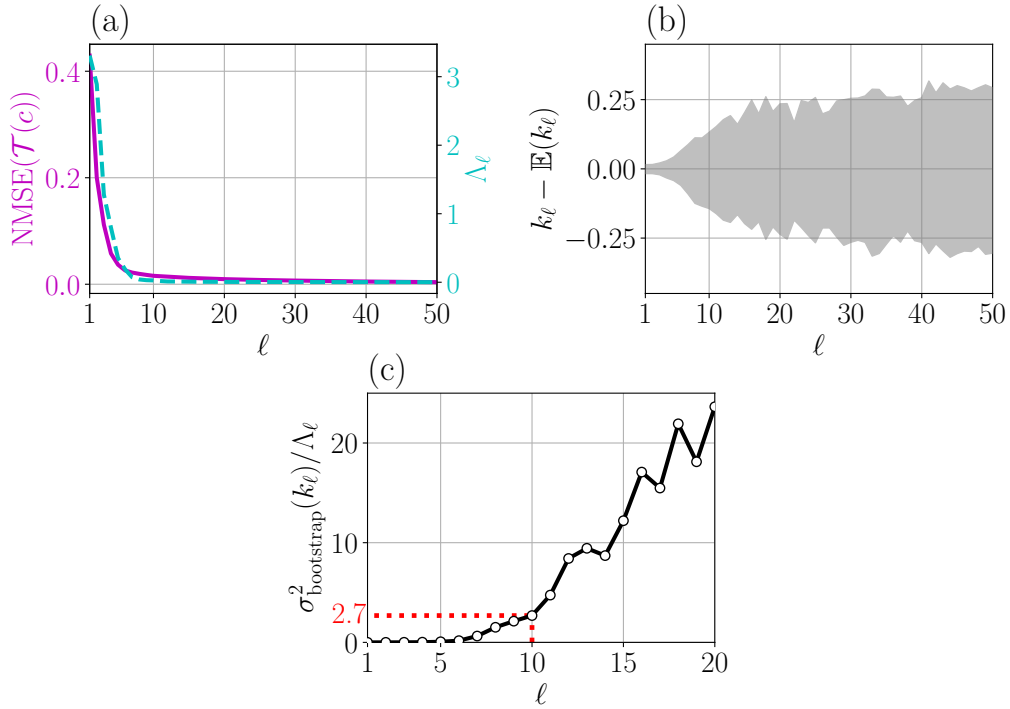


Figure 5: (a) POD projection error evaluated over the train set with NMSE (Eq. 15) as function of the number of modes retained, and POD eigenvalues Λ_ℓ associated with each mode ℓ . (b) Spread of the difference between POD reduced coefficients k_ℓ replicates and their mean $\mathbb{E}(k_\ell)$. The spread is defined by the 2.5th and 97.5th percentiles and is averaged over the train set. (c) Ratio between the averaged variance of the reduced coefficient bootstrap replicates $\sigma_{\text{bootstrap}}^2(k_\ell)$ and the POD eigenvalue Λ_ℓ associated with each mode ℓ . The red dotted line indicates the number of modes selected for this study.

434 **Internal variability in the POD latent space** To quantify how the noise caused by
435 internal variability is captured by each POD mode, we project the bootstrap replicates of
436 the LES fields onto the POD latent space constructed with the original fields (Sect. 2.5).
437 We thereby obtain 1,000 realizations of the POD reduced coefficients k_ℓ associated with
438 each field in the dataset. Figure 5b shows that the spread of the reduced coefficient
439 replicates increases significantly when going to higher order modes (i.e. for increasing ℓ).
440 In particular, for $\ell \leq 5$, the spread of the bootstrap replicates of the reduced coefficients
441 remain small ($< 10\%$), implying that these modes correspond to systematic patterns
442 associated with the plume structure and its dependence on the wind conditions. The
443 variability of the POD reduced coefficients then increases rapidly before reaching a plateau
444 from $\ell \geq 15$. At this plateau, the spread of the k_ℓ replicates varies by about $\pm 25\%$. This
445 implies that field features linked to internal variability are mainly captured by higher
446 order modes, which is consistent with the literature (Forkman et al. 2019). This in turn
447 implies that we need to limit the number of modes L to avoid introducing noise into the
448 POD-GPR surrogate model.

449 **A priori criterion to choose the POD latent space dimension** Based on these
450 findings, we propose to measure the ratio between the internal variability noise and the
451 fraction of the total ensemble variance represented by each mode defined as

$$\frac{\sigma_{\text{bootstrap}}^2(k_\ell)}{\Lambda_\ell}, \quad (14)$$

452 where $\sigma_{\text{bootstrap}}^2(k_\ell)$ is the variance of the POD reduced coefficients replicates averaged
453 over the train set, and where Λ_ℓ is the ℓ th eigenvalue in the POD decomposition.

454 The ratio in Eq. 14 is shown in Fig. 5c and provides a way to choose the latent space
455 dimension L that minimizes both the noise and the POD projection error, and it has the
456 advantage of being completely a priori as it does not require either the test set or the
457 evaluation of the full POD-GPR model. Results show that this ratio is close to zero for
458 the first six modes and then increases sharply with mode order. We therefore choose to
459 truncate the POD decomposition before the inflection point using $L = 10$ modes to project

460 the mean concentration fields. This approach for selecting the latent space dimension is
 461 evaluated a posteriori in Sect 4.3.

462 3.5 Surrogate validation methodology

463 We present now the metrics used to quantify the surrogate model reduction error,
 464 before estimating the best values achievable for each metric given the internal variability.

465 3.5.1 Quantification of the surrogate error

466 The POD–GPR model accuracy is estimated on a set of independent test samples
 467 ($N_{test} = 40$, corresponding to 20% of the full LES dataset, see Fig. 1). This is essential
 468 to assess the ability of the model to generalize information from the train set to new
 469 meteorological forcing parameters (α_{inlet} , u_*).

470 To assess the surrogate error, we use standard air quality metrics from Chang and
 471 Hanna (2004). These metrics compare the mean concentration field predicted by the
 472 surrogate model $\mathbf{c}_{surrogate}$ with the LES counterpart \mathbf{c}_{LES} in terms of normalized mean
 473 square error (NMSE), fraction of predictions within a factor of two of observations (FAC2),
 474 geometric variance (VG), and figure of merit in space (FMS):

$$NMSE = \frac{\langle (\mathbf{c}_{LES} - \mathbf{c}_{surrogate})^2 \rangle}{\langle \mathbf{c}_{LES} \rangle \langle \mathbf{c}_{surrogate} \rangle}, \quad (15)$$

$$FAC2 = \langle \xi \rangle \text{ with } \xi(\mathbf{x}_k) = \begin{cases} 1 & \text{if } 0.5 \leq \mathbf{c}_{surrogate}(\mathbf{x}_k) / \mathbf{c}_{LES}(\mathbf{x}_k) \leq 2, \\ 1 & \text{if } \mathbf{c}_{surrogate}(\mathbf{x}_k) \leq c_t \text{ and } \mathbf{c}_{LES}(\mathbf{x}_k) \leq c_t, \\ 0 & \text{else,} \end{cases} \quad (16)$$

$$VG = \exp \left(\langle (\ln \tilde{\mathbf{c}}_{LES} - \ln \tilde{\mathbf{c}}_{surrogate})^2 \rangle \right), \quad (17)$$

$$FMS(c_\ell) = \frac{\Omega_\cap(c_\ell)}{\Omega_\cup(c_\ell)}, \quad (18)$$

478 where $\langle \cdot \rangle$ denotes spatial averaging weighted by the dual volume of the node \mathbf{x}_k , c_t is
 479 a concentration threshold defining $\tilde{\mathbf{c}} = \max(\mathbf{c}, c_t)$, as suggested by Chang and Hanna

480 (2004) and Schatzmann et al. (2010) to avoid issues with values close to zero in FAC2
 481 and VG metrics. In this study, we use $c_t = 10^{-4}$ ppm, considering that errors on lower
 482 concentrations are mainly due to numerical noise. Finally, $\Omega_{\cap}(c_\ell)$ denotes the volume, in
 483 m^3 , of the domain in which both $\mathbf{c}_{\text{surrogate}}$ and \mathbf{c}_{LES} are over a user-specified tracer value
 484 c_ℓ . Conversely, $\Omega_{\cup}(c_\ell)$ denotes the volume where $\mathbf{c}_{\text{surrogate}} \geq c_\ell$ or $\mathbf{c}_{\text{LES}} \geq c_\ell$.

485 The use of different metrics than the loss used during training is important because
 486 of the multi-order nature of the concentration field. NMSE is more sensitive to errors at
 487 high concentrations, while VG assesses prediction accuracy at low concentrations. FMS
 488 quantifies how close the two plume shapes are relative to a given concentration level. The
 489 scores that a perfect model would obtain are reported in Table 1.

490 3.5.2 Estimation of the internal variability

491 LES data are noisy due to internal variability (Sect 2.5). It would therefore be pointless
 492 to try to build a surrogate model whose accuracy exceeds this uncertainty. To quantify
 493 the error due to internal variability alone, we use the bootstrap approach proposed in
 494 Lumet et al. (2024b) to generate two independent sets of bootstrap replicates of the same
 495 LES field. We then compute the average difference between each pair of replicates using
 496 the metrics introduced in Sect. 3.5.1. For each metric, we obtain the amount of error due
 497 to internal variability only, which is the expected error when comparing two independent
 498 realizations of the mean concentration fields for the same input parameters.

499 This is done for every LES sample in the dataset, and the ensemble-averaged internal
 500 variability errors give an upper bound estimate of the best overall accuracy achievable for
 501 each metric when validating the POD–GPR surrogate model.

502 4 Surrogate model validation

503 In this section, we present a thorough evaluation of the POD–GPR surrogate model.
 504 We first assess its accuracy over the test set and its efficiency (Sect. 4.1). We then validate
 505 the innovative aspects of our approach: the POD–GPR uncertainty estimation (Sect. 4.2),
 506 and the selection of the number of POD modes (Sect. 4.3). Finally, we study how the

507 POD–GPR model behaves when reducing the train set (Sect. 4.4). All results are given
 508 for the mean concentration field, but the POD–GPR approach can be applied to any LES
 509 field (Lumet (2024), Appendix B).

510 4.1 Evaluation of the surrogate model field predictions

511 We evaluate here the POD–GPR predictions of mean concentration following the
 512 methodology introduced in Sect. 3.5, using the mean internal variability error as the
 513 reference for validation. We use a latent space dimension of $L = 10$ in accordance with
 514 the informed choice made in Sect. 3.4.

515 **Prediction accuracy** The overall performance of the surrogate model is quantified us-
 516 ing standard air quality metrics (Sect. 3.5.1). Table 1 shows the obtained scores averaged
 517 over the test set. Overall, the POD–GPR model yields very satisfactory results, with
 518 most scores close to the error due to internal variability only, which is the best achievable
 519 accuracy. However, the results for NMSE and FMS(1 ppm) remain relatively far from
 520 the internal variability error, indicating that POD–GPR is less good at predicting high
 521 concentration values.

Table 1: *Prediction accuracy of the POD–GPR surrogate model evaluated using the metrics de-
 fined in Sect. 3.5.1 and averaged over the test set. The standard deviations of the scores over the
 test set are also given, as well as the individual scores for test samples #81 and #187, which repre-
 sent the lowest and highest FAC2 scores achieved by the POD–GPR, respectively. For comparison,
 the perfect scores for the metrics, the mean error due to internal variability only (Sect. 3.5.2) and
 the mean error due to standalone reduction dimension are given.*

	FAC2	NMSE	VG	FMS (1 ppm)	FMS (0.01 ppm)
Perfect score	1	0	0	1	1
Internal variability	0.95	1.80	1.39	0.83	0.93
POD projection error	0.91	20.4	1.33	0.75	0.93
POD–GPR prediction error	0.91	20.6	1.39	0.75	0.92
Standard deviation	0.04	43.2	0.68	0.11	0.03
Test sample #81	0.74	23.4	5.25	0.79	0.85
Test sample #187	0.96	8.08	1.07	0.86	0.94

522 Table 1 also shows that the POD–GPR prediction errors are almost identical to the

standalone POD projection errors (i.e. errors obtained by simply reconstructing the test fields after projection onto the POD basis by inverse POD transformation). This implies that the accuracy of the POD–GPR model is mostly limited by the accuracy of the POD and not by the GPR. In addition, the poor prediction performance for high concentrations can be explained by the fact that the POD is not well adapted to the multiscale and nonlinear nature of the concentration fields. In particular, the use of a logarithmic preprocessing before the POD degrades the reconstruction of high concentrations in the vicinity of the emission source, but has the advantage of preserving the other metrics and in particular the shape of the plume compared to linear processing (Lumet (2024), Chapter IV).

There is quite a large spread of POD–GPR errors across the test samples, especially for the quadratic metrics NMSE and VG, indicating the presence of test sample outliers. This variability over the input parameter space is mainly explained by the fact that as the friction velocity decreases, the internal variability increases (Fig. 3), which makes the mean concentration noisier and therefore more difficult to predict. In addition, FMS(1 ppm), and to a lesser extent FMS(0.01 ppm) and FAC2, are subject to a zoning effect as they depend on the size of the plume within the domain of interest (Eqs. 16, 18). For example, these scores are improved when the wind direction carries the plume outside the container array (i.e. for $\alpha_{inlet} \approx 30^\circ$ or $\alpha_{inlet} \approx -90^\circ$).

Field prediction examples For a more detailed assessment of the POD–GPR model accuracy, we also examine its predictions in the physical space. Figures 6a, b, c, and d compare 2-D cuts of the mean concentration at $z = 1.6$ m predicted by LES and POD–GPR. Results are given for the test sample #187 $(\alpha_{inlet}^{(187)}, u_*^{(187)}) = (21.8^\circ, 0.59 \text{ m s}^{-1})$ for which POD–GPR obtains the best FAC2 score over the test set, and for the test sample #81 $(\alpha_{inlet}^{(81)}, u_*^{(81)}) = (-27.7^\circ, 0.08 \text{ m s}^{-1})$ associated with the worst FAC2 score. The global scores obtained for these two particular snapshots are summarized in Table 1.

In both cases, the POD–GPR model reproduces well the main features of the LES concentration field, in particular the shape and orientation of the plume. The spatial

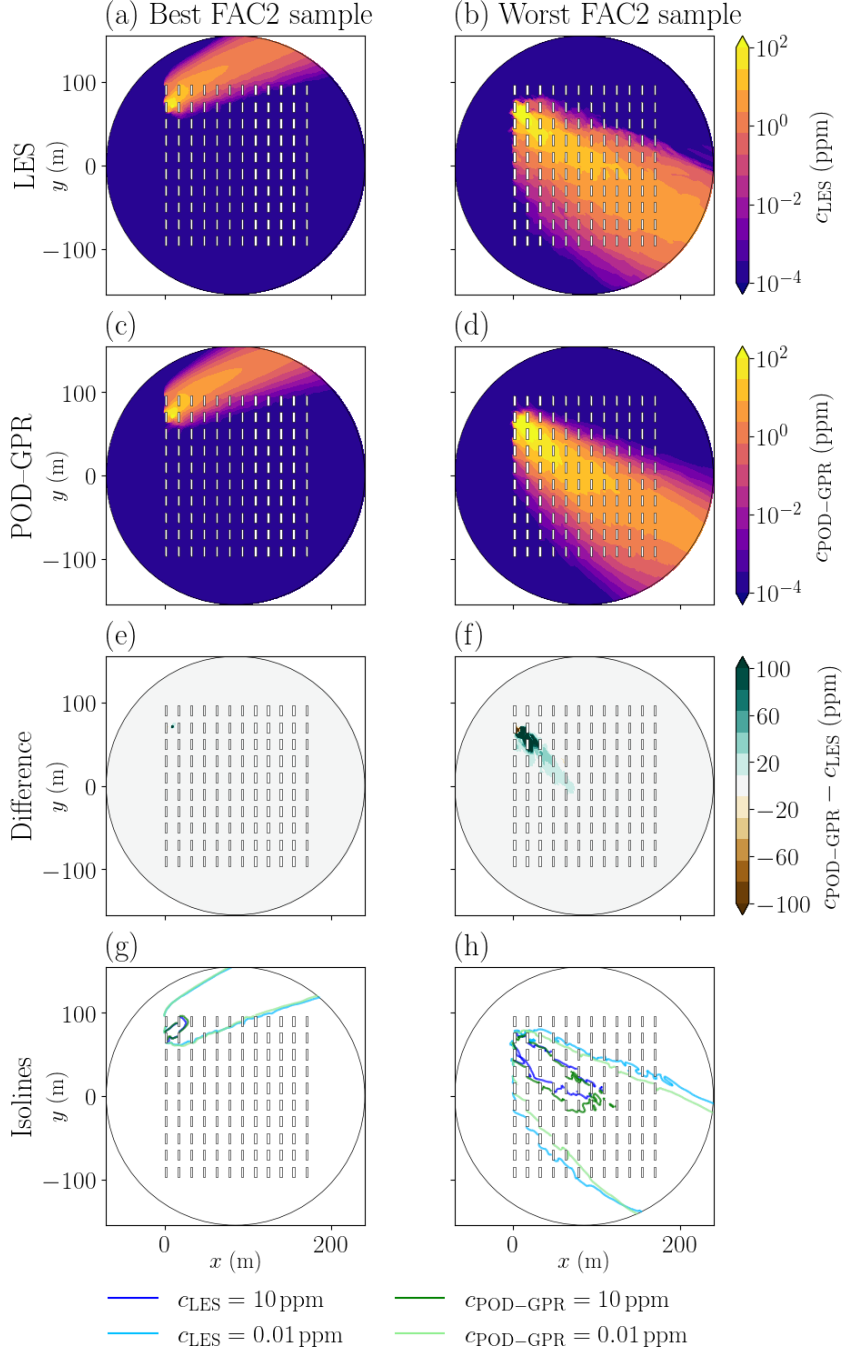


Figure 6: Horizontal cuts at $z = 1.6$ m of two test mean concentration fields estimated by LES (a, b) and POD-GPR (c, d), and the absolute difference between the two (e, f). The left column corresponds to the test sample #187 for which POD-GPR achieves the best FAC2 (Eq. 16) score over the test set, and the right column corresponds to the test sample #81 which is associated with the worst FAC2 score. The LES and POD-GPR predictions of 0.01 ppm and 10 ppm iso concentration levels are shown in (g, h).

551 distribution of the different concentration levels is also well reproduced, which is confirmed
552 by the near superposition of the 0.01 ppm and 10 ppm concentration contour lines between
553 LES and POD-GPR (Fig. 6d, h).

554 However, for the sample with the worst FAC2 (#81), the POD-GPR underestimates
555 the spanwise spread of the plume and significantly overestimates the mean concentration
556 near the emission source (Fig. 6g). This is consistent with the poor NMSE obtained
557 (Table 1) and this is due to the poor reproduction of high concentrations by the POD
558 with logarithmic preprocessing. For this sample (corresponding to a low friction velocity
559 and therefore subject to substantial internal variability) the POD-GPR tends to smooth
560 the irregularities observed at the edges of the plume, thus poorly predicting the local
561 abrupt decrease in concentration.

562 **Efficiency** In terms of computational cost, it takes approximately 30s to train the
563 POD-GPR model using a single core of an Intel Ice Lake CPU. This includes field pre-
564 processing, POD basis decomposition and GPR optimization. This training cost is in-
565 significant compared to the cost of building the training dataset (Sect. 2.4). Once trained,
566 the model provides a prediction of the full 3-D concentration field in about 0.03 s. This ap-
567 proach is therefore compatible with applications requiring a large ensemble of predictions
568 and/or real-time predictions.

569 4.2 Assessment of the surrogate model uncertainty estimation

570 We evaluate here the ability of the POD-GPR model to provide realistic uncertainty
571 estimates by comparing them to the actual surrogate error over the test set and to the
572 internal variability present in the LES dataset.

573 **Uncertainty reliability** Figure 7a shows the uncertainty reliability diagram comparing
574 actual surrogate error (y -axis) and surrogate model uncertainty estimates (x -axis). The
575 POD-GPR uncertainty is underestimated compared to the actual POD-GPR error for
576 most domain nodes, especially for the lowest concentration values. Nevertheless, the
577 estimated trend is consistent, i.e. the larger the actual error, the larger the prior estimate.

578 Furthermore, the overall level of precision is satisfactory as the estimated uncertainty is
579 in the right order of magnitude (within the green dashed lines) for 98% of the domain
580 nodes. This is confirmed by the response surface of the POD–GPR (Fig. 12a, b), as the
581 predicted envelopes appear to cover the test samples well. We can therefore be confident
582 in the uncertainty predicted by the POD–GPR surrogate model despite a tendency to
583 underestimate.

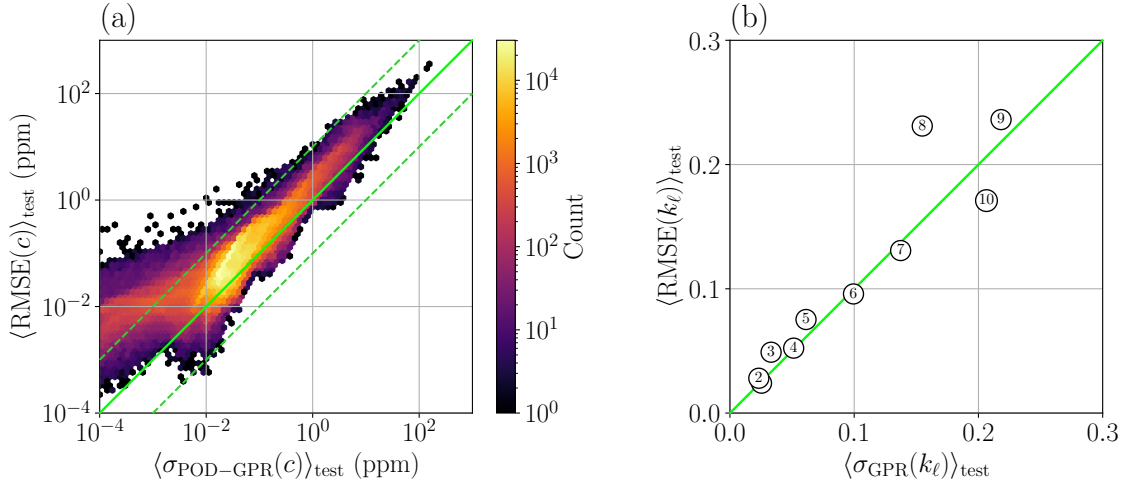


Figure 7: Reliability diagrams in the physical space and in the latent space: (a) Root mean square error (RMSE) of the POD–GPR concentration prediction over the test set versus the POD–GPR estimated uncertainty at each node where the concentration is larger than the tolerance $c_t = 10^{-4}$ ppm. Each hexagon is colored according to the number of node points in the hexagon. (b) RMSE of the GP prediction of the POD reduced coefficients k_ℓ over the test set versus the GP estimated uncertainty, each mode ℓ is represented by a numbered circle (the POD latent space dimension is $L = 10$). The green solid lines correspond to the identity function, and the dashed lines in (a) show the range of plus or minus one order of magnitude.

584 To further investigate the cause of this underestimation, the uncertainty reliability is
585 examined directly in the latent space in Fig. 7b. We find that for the estimation of the
586 reduced POD coefficients by the GPs, the uncertainty estimate is very close to the error
587 made on average, except for the high-order modes 8 and 10. This increase in error for
588 higher-order modes is consistent with the fact that they are more affected by internal
589 variability (Fig. 5b). The following conclusions can be drawn: i) the variance of the GP
590 posterior distribution (Eq. 10b) is realistic, and ii) the underestimation observed in the
591 physical space in Fig. 7a comes from the inverse POD projection. This is consistent with
592 the fact that the POD projection error is not taken into account when estimating the

593 total POD–GPR uncertainty (Sect. 3.3), yet the total POD–GPR error is essentially due
 594 to the POD projection error as indicated in Table 1.

595 **Ability to estimate internal variability a posteriori** We now examine the nature
 596 of the estimated uncertainty in more detail, and assess the proportion due to internal
 597 variability. The first point is to study how the noise of the LES fields projected onto
 598 the POD latent space is captured by GPR. Figure 8 shows that the values of the GP
 599 variance hyperparameters s_ℓ^2 obtained by maximum likelihood estimation are very close
 600 to the maximum level of internal variability of the POD reduced coefficients over the train
 601 set estimated by bootstrap. This is a strong result because the bootstrap estimates of the
 602 internal variability are not used to train the GPs.

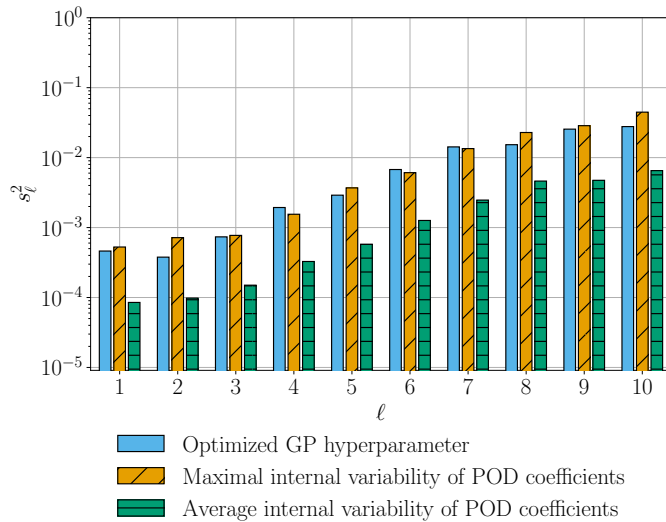


Figure 8: GP noise variance s_ℓ^2 hyperparameter obtained by log-likelihood maximization for each mode ℓ as blue bars, and maximal (resp. average) noise on the POD reduced coefficients over the train set as orange (resp. green) bars.

603 The fact that the GP noise variance parameter matches the maximum level of inter-
 604 nal variability (Fig. 8) implies that GPs overestimate the variance of the POD reduced
 605 coefficients for most samples where the internal variability is low. This is a structural
 606 limitation due to the fact that the GP additive noise does not depend on the input pa-
 607 rameter space (Eq. 8), while the variance due to internal variability does (Fig. 3). As
 608 a result, in the physical space, the POD–GPR uncertainty predictions tend to be un-

609 derestimated compared to the actual internal variability for samples where the internal
 610 variability is high, while they are overestimated for samples with low internal variability.
 611 This could be partially overcome in the future by implementing input-dependent noise
 612 variance hyperparameters, as suggested by Miyagusuku et al. (2015).

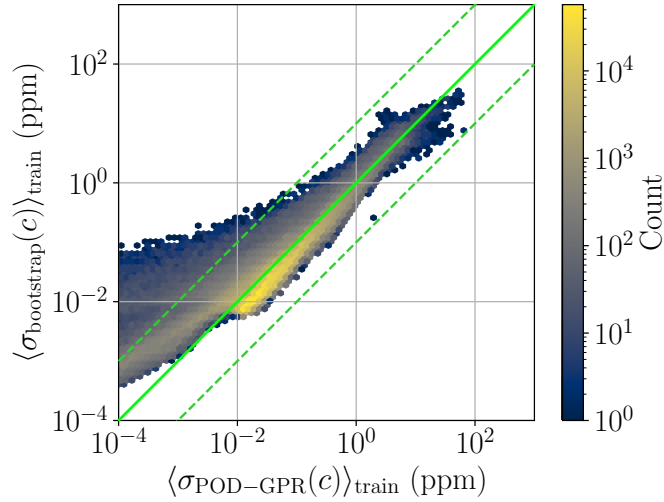


Figure 9: Internal variability of the mean concentration estimated by bootstrap and averaged over the train set versus the POD-GPR estimated uncertainty at each node where the concentration is larger than the tolerance $c_t = 10^{-4}$ ppm. Each hexagon is colored according to the number of node points in the hexagon. The green solid lines correspond to the identity function and the dashed lines show the range of plus or minus one order of magnitude.

613 Figure 9 shows that the uncertainty estimated by the POD-GPR is overall consistent
 614 with the LES internal variability over the train set, as the level of variability is in the right
 615 order of magnitude for 99% of the domain nodes. For most of the domain, the POD-GPR
 616 tends to overestimate the internal variability (hexagonal cells of high density beyond the
 617 green line), which is consistent with the GP noise matching the maximum level of internal
 618 variability in the latent space (Fig. 8). Note that this analysis is performed over the train
 619 set since for these samples the GPR regression covariance is zero, and thus the POD-
 620 GPR uncertainty estimate only corresponds to the estimated internal variability. Finally,
 621 we note that the estimated uncertainty envelopes are consistent with the LES internal
 622 variability when looking at the POD-GPR response surfaces (Fig. 12a, b).

623 In this internal variability analysis, the second point is to evaluate the spatial con-
 624 sistency of the POD-GPR uncertainty estimates with respect to the spatial distribu-

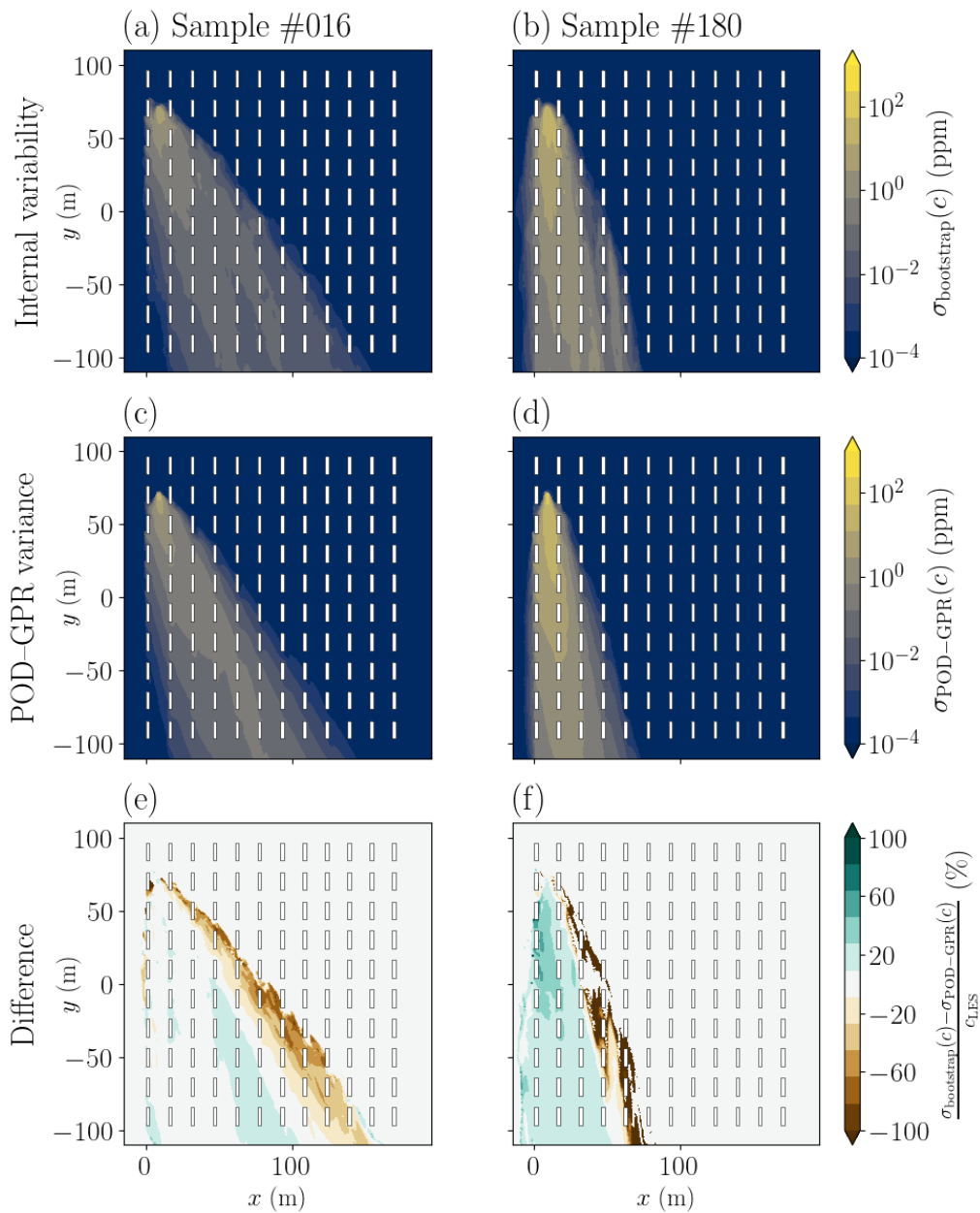


Figure 10: Horizontal cuts at $z = 1.6$ m of the standard deviation of the mean concentration induced by internal variability estimated using bootstrap (a, b), predicted by POD-GPR (c, d), and the relative difference between the two (e, f). The left column corresponds to the train sample #016 and the right column corresponds to the train sample #180

625 tion of internal variability to verify that the uncertainty is properly propagated from
 626 the POD latent space to the physical space (Sect. 3.3). We find that the variance
 627 predicted by the POD-GPR is consistent with the internal variability of the LES in
 628 terms of magnitude and structure, as shown in Fig. 10 for the train sample #016

629 $\left(\alpha_{inlet}^{(016)}, u_*^{(016)}\right) = (-79.5^\circ, 0.14 \text{ m s}^{-1})$ for which the POD–GPR uncertainty estimate
 630 is the closest to the internal variability estimated by bootstrap and for the train sample
 631 $\#180 \left(\alpha_{inlet}^{(180)}, u_*^{(180)}\right) = (-58.1^\circ, 0.56 \text{ m s}^{-1})$, where POD–GPR overestimates the internal
 632 variability the most. Despite the overall agreement, the POD–GPR variability estimates
 633 appear to be overestimated within the plume and significantly underestimated near the
 634 plume edges (Fig. 10e, f), which is consistent with the overall tendency to underestimate
 635 low internal variability levels (Fig. 9). This is explained by the fact that there are high
 636 concentration gradients near the plume edges and thus high internal variability levels,
 637 a feature not well represented by the POD projection, which is based solely on mean
 638 concentration and not on its variability.

639 **In summary,** the POD–GPR uncertainty estimates derived in Sect. 3.3 i) represent, in a
 640 spatially coherent manner, the inherent internal variability of the mean concentration field
 641 thanks to the ability of the GPs to accurately infer the level of noise in the train set, and
 642 ii) properly explain the actual surrogate errors at predicting the mean concentration. This
 643 particularly reinforces the robustness of the POD–GPR and its relevance to uncertainty
 644 quantification applications.

645 4.3 A posteriori validation of the latent space dimension

646 We revisit our choice of the number of POD modes ($L = 10$) obtained by following
 647 the a priori statistical approach we propose in Sect. 3.4. For this purpose, we evaluate
 648 the effect of the number of modes L on the performance of the full POD–GPR model on
 649 the test set (i.e. by varying L from 5 to 50 in the construction of the POD–GPR model).

650 **Validation metrics** Figure 11 shows how the metrics defined in Sect. 3.5.1 change
 651 when modifying the POD latent space dimension L . The POD–GPR prediction accuracy
 652 over the test set increases with the number of modes and reaches a plateau for a larger
 653 number of modes ($L \approx 15\text{--}25$) than the NMSE on the train set used in our mode choice
 654 approach (Fig. 5). This may indicate that integrating a larger number of modes into the
 655 POD–GPR model could lead to improved surrogate model accuracy.

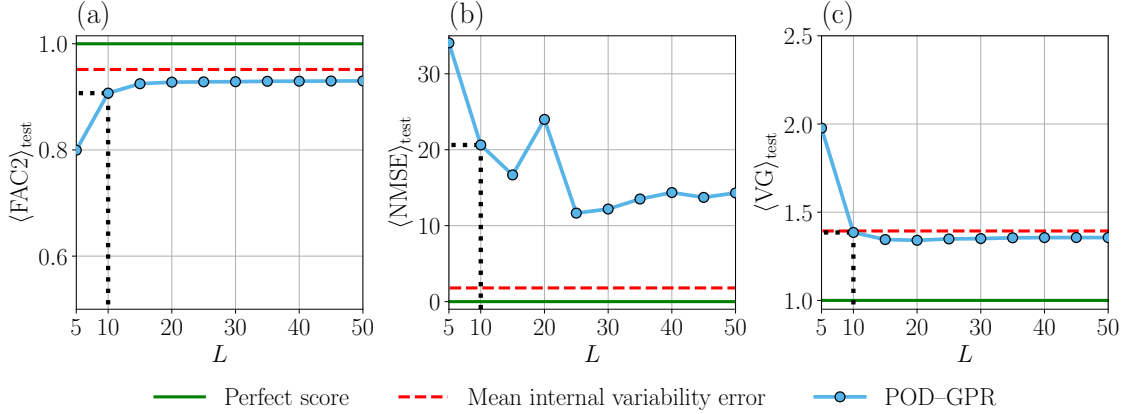


Figure 11: *POD-GPR prediction error as a function of the number of the modes L and evaluated with FAC2 (a), NMSE (b), VG (c) averaged over the test set. Green lines correspond to perfect scores; and red dashed lines correspond to the mean level of error due to internal variability only. Error levels corresponding to the selected number of modes ($L = 10$) are shown as black dotted lines.*

656 **Response surfaces** As an additional diagnostic, Fig. 12 shows that using a larger
657 number of modes significantly deteriorates the POD-GPR response surfaces, making them
658 very noisy and implausible as, with $L = 50$ modes (Fig. 12e, f), the POD-GPR model is no
659 longer able to retrieve the inversely proportional dependence of concentration on friction
660 velocity expected from theory and retrieved for the configuration with $L = 10$ modes
661 (Fig. 12a, b). This degradation is due to the fact that high-order modes mostly account
662 for noisy structures due to internal variability (Fig. 5b), and are therefore not informative
663 on systematic structures related to the wind conditions. As a result, when including high-
664 order modes, the GPs attempt to learn unphysical dependence on the input parameters,
665 resulting in the shortwave noise observed in Fig. 12. Still, the increase in uncertainty with
666 the response surface deterioration suggests that the POD-GPR uncertainty estimate is
667 robust. However, the fact that the degradation of the POD-GPR response surface is not
668 seen by the global metrics, which continue to improve as the number of modes increases
669 (Fig. 11), shows that one should not draw conclusions based on scalar metrics alone.

670 In the light of these tests, our prior selection method for the latent space dimension is
671 convincing. The resulting trade-off of $L = 10$ yields good validation scores, while avoiding
672 the problem of response surface noise. However, we acknowledge that using a slightly
673 larger number of modes ($L \approx 15-20$) would also be appropriate and even slightly improve

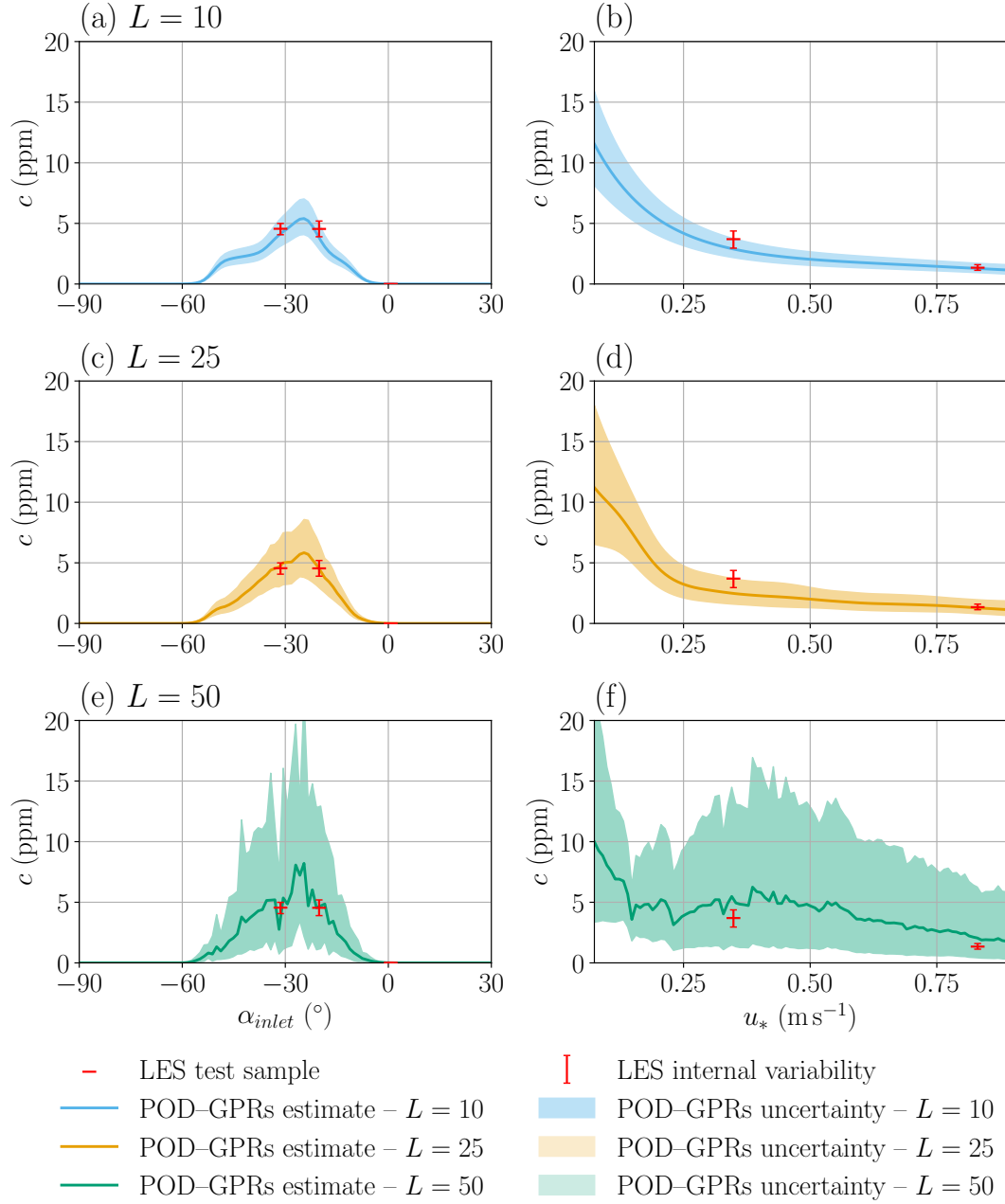


Figure 12: *POD-GPR prediction of the mean concentration at tower B at $z = 2$ m (see tower location in Fig. 2) as a function of the inlet wind direction α_{inlet} (a, c, e), and of the friction velocity u_* (b, d, f). Shaded areas correspond to the 95% confidence intervals estimated by the POD-GPR according to the procedure detailed in Sect. 3.3. Each row corresponds to the results obtained with a different latent space dimension $L \in \{10, 25, 50\}$. When varying one parameter, the other is set constant to either $u_*^{plot} = 0.45 \text{ m s}^{-1}$ (a, c, e), or $\alpha_{inlet}^{plot} = -43^{\circ}$ (b, d, f), and the test samples closest to the two segments of parameter space thus scanned (see Fig. 1) are represented by horizontal red bars. The uncertainty on LES test samples induced by internal variability is depicted as red vertical error bars.*

674 the surrogate model accuracy. Defining an optimal criterion for latent space dimension
675 selection based on the noise/signal ratio defined in Eq. 14 is therefore an interesting
676 prospect, but requires more validation cases.

677 4.4 Robustness to training set reduction

678 In order to assess the potential of the POD–GPR approach for future applications,
679 we examine how the POD–GPR accuracy evolves as the size of the train set decreases
680 (without changing the test set). This is particularly important to investigate the possi-
681 ble trade-offs between the ability of the model to generalize from training data and the
682 substantial cost of building the LES training dataset.

683 The surrogate model is trained for decreasing train set sizes from $N_{train} = 160$ to
684 $N_{train} = 40$ by keeping only the first samples in Halton’s sequence. To make the compar-
685 ison fair, we systematically evaluate the averaged prediction errors over the same test set
686 of $N_{test} = 40$ samples. Results are shown in Fig. 13a, b, c and d in terms of FAC2, VG,
687 FMS(1 ppm), FMS(0.01 ppm). The decrease in accuracy is fairly constrained and evolves
688 linearly with the train set size, with a loss of 0.08 in FAC2 and 0.12 in VG for every 10
689 training samples removed. More importantly, the accuracy decreases less rapidly than
690 that of the nearest neighbor model (1–NN), which trivially predicts the mean concentra-
691 tion field as equal to the closest train field in the parameter space (see Appendix). This
692 is especially true for the low concentration values, as the VG score is significantly higher
693 with the 1–NN model than with the POD–GPR model for small train set sizes (Fig. 13b).

694 Regarding the NMSE metric (Fig. 13e), the evolution with N_{train} is quite chaotic for
695 the POD–GPR and worse than for the 1–NN approach. As previously mentioned, this
696 is related to the high POD projection error near the source when using the logarithmic
697 transformation, and we can consider that the POD–GPR approach with the present pre-
698 processing is not designed to make predictions near the source, regardless of the train set
699 size.

700 Figure 14 shows that the POD–GPR uncertainty predictions are very robust to train set
701 size reduction. We find that, on average, the POD–GPR uncertainty predictions explain

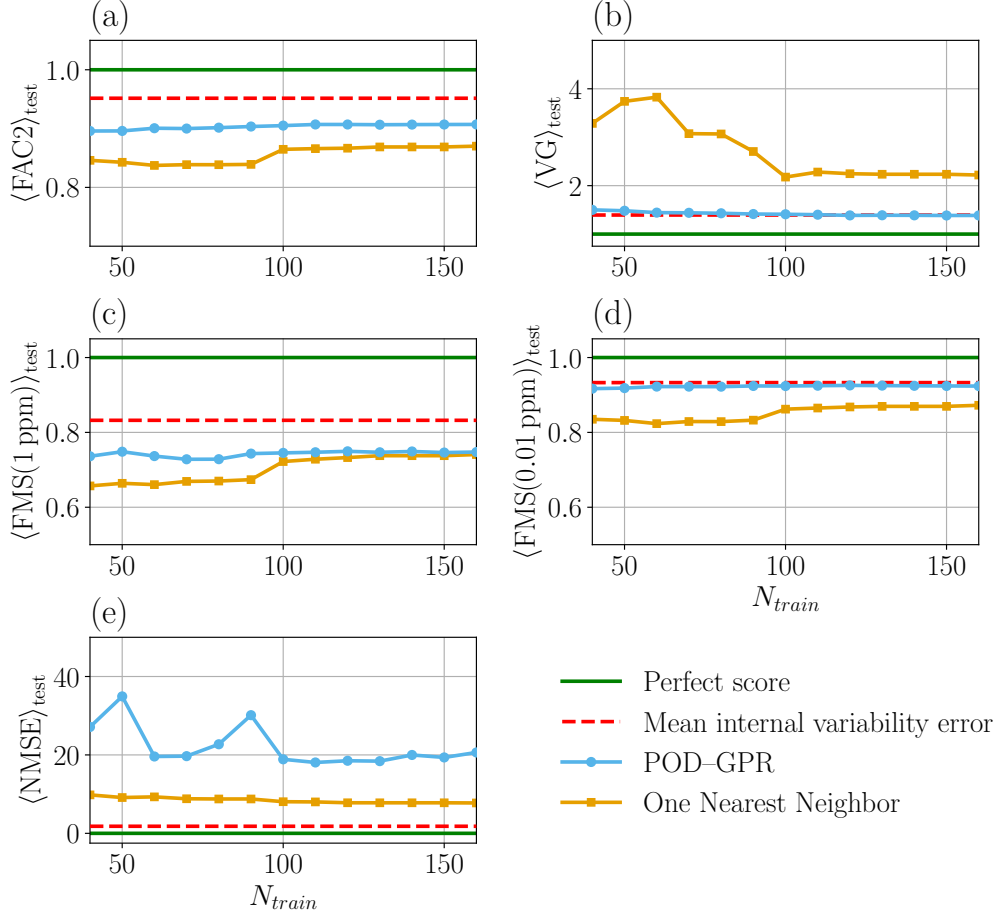


Figure 13: Surrogate modeling errors for decreasing train set sizes. The mean concentration prediction error is assessed using the metrics defined in Sect. 3.5.1: namely FAC2 (a), VG (b), FMS (c, d), and NMSE (e). Results are given for the POD-GPR as blue circles and the 1-NN model as orange squares. Perfect scores are represented as green lines; and red dashed lines correspond to the mean level of error due to internal variability only.

702 overall well its actual error over the test set even with only 40 train samples (Fig. 14a,
703 b, c). Similarly, the ability of the POD-GPR to represent the internal variability of the
704 mean concentration is well preserved (Fig. 14d, e, f), although we note a tendency to
705 underestimate it when the train set size is reduced, as there are fewer close neighboring
706 points for the GPs to estimate the noise in this case.

707 In summary, the ability of the POD-GPR model to generalize from a training dataset
708 of limited size is better than for the 1-NN baseline approach, justifying the use of such
709 a more sophisticated surrogate model. We find that for this problem, 40 LES training
710 samples are sufficient to achieve good levels of accuracy for most metrics. Furthermore,

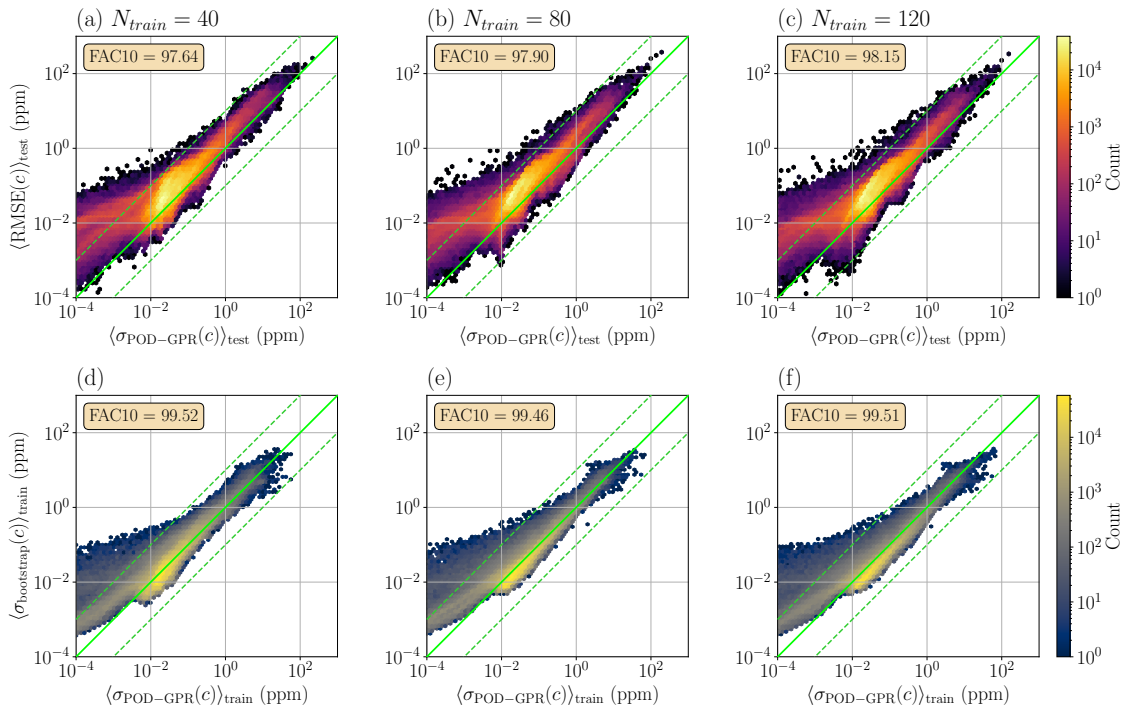


Figure 14: Reliability diagrams of the POD–GPR uncertainty estimates for varying train set size $N_{\text{train}} \in \{40, 80, 120\}$. (a, b, c) Root mean square error (RMSE) of the POD–GPR concentration prediction over the test set and (d, e, f) internal variability of the mean concentration estimated by bootstrap and averaged over the train set, both versus the POD–GPR estimated uncertainty at each node where the concentration is larger than the tolerance $c_t = 10^{-4}$ ppm. Each hexagon is colored according to the number of node points in the hexagon. The green solid lines correspond to the identity function and the dashed lines show the range of plus or minus one order of magnitude. The FAC10 scores give the percentage of points between the two dashed lines (similarly as in Eq. 16).

711 the uncertainty estimates provided by POD–GPR remain consistent as the training set
 712 size decreases, despite a tendency to overestimate.

713 5 Conclusion

714 In this study, a data-driven surrogate dispersion model based on the two-stage POD–
 715 GPR approach was trained and rigorously evaluated using a large dataset of 200 LES
 716 simulations reproducing microscale dispersion scenarios of the field-scale MUST experi-
 717 ment for varying meteorological forcing. The resulting surrogate model is able to capture
 718 well the general plume shape within the canopy, approaching the best achievable accuracy
 719 given the internal variability in the LES data, while being very computationally efficient.

720 The main novelty of this study is the in-depth analysis of the POD-GPR surrogate

721 model uncertainty and of the weight of internal variability, thus meeting the need ex-
722 pressed by Dauxois et al. (2021); Tominaga et al. (2023) and Wu and Quan (2024).
723 Future developments are required to account for the POD projection error in the POD-
724 GPR uncertainty estimate to avoid error underestimation. But the present uncertainty
725 estimates already explain the differences between the POD-GPR predictions and the LES
726 references quite well, being in the right order of magnitude in 97% of cases. This work
727 thus represents an important methodological step towards the representation of total un-
728 certainty in microscale urban pollutant dispersion, as aleatory and modeling uncertainties
729 have not been considered in most uncertainty quantification (García-Sánchez et al. 2014,
730 2017) and data assimilation (Xiao et al. 2016; Mons et al. 2017; Sousa et al. 2018; Sousa
731 and Gorlé 2019; Defforge et al. 2019, 2021) studies to date.

732 A second important contribution of this study is the method for selecting a priori the
733 POD latent space dimension, which is based on a trade-off between the accuracy of the
734 POD reconstruction and the noise captured by the POD modes estimated by bootstrap
735 as in Lumet et al. (2024b). The threshold used here to make this trade-off need to be
736 consolidated and made more objective in future studies by considering a wide range of
737 cases. For this study, the retained dimension ($L = 10$) is smaller than the dimension
738 chosen based on the standalone reconstruction error (Xiao et al. 2019; Nony et al. 2023),
739 but this choice is justified by the fact that using more modes ($L > 25$) significantly noises
740 and degrades the POD-GPR response surface despite slightly better global metrics such
741 as FAC2 and NMSE. This highlights that a surrogate model validation process learning
742 from LES data, especially for the concentration variable, should not be based solely on
743 global metrics but requires more local and structural analyses.

744 In this study, the main shortcoming of the POD-GPR approach is its lack of accuracy
745 in areas of high concentration, i.e. close to the source. This is mainly due to POD, as
746 a linear transformation is not well suited to the wide disparity in concentration scales
747 and introduces projection errors. A promising way to overcome this issue is the mixture-
748 of-experts approach (El Garroussi et al. 2020), whose key idea is to train several POD-
749 GPR models, each corresponding to a different preprocessing, to capture the different

750 concentration scales (Lumet (2024), Appendix B). Another promising perspective is the
751 use of nonlinear dimension reduction techniques such as neural network autoencoders
752 (Murata et al. 2020; Xiang et al. 2021; Masoumi-Verki et al. 2022; Nony 2023). However,
753 a difficulty lies in the interpretation of the nonlinear latent space and in the identification
754 of the internal variability noise.

755 In the future, using deep learning for dimension reduction and/or learning the de-
756 pendency on new parameters such as the source location will require significantly larger
757 training datasets, which may not be feasible due to the computational cost of LES. Defin-
758 ing the minimum amount of LES data required for training is therefore a key issue in
759 LES emulator development. In this study, the POD–GPR surrogate model copes very
760 well with a reduction of the train set down to 40 samples for two input parameters.
761 The number of training samples may be further reduced by applying adaptive sampling
762 methods to target learning zones (Picheny et al. 2010; Braconnier et al. 2011). Multif-
763 delity approaches (Lamberti and Gorlé 2021; Nony 2023) are also promising to to enrich a
764 train set by including information from a lower fidelity, lower cost model, while retaining
765 the more accurate information provided by LES, thus paving the way for the use of the
766 uncertainty-aware POD–GPR surrogate model for more general and more complex urban
767 pollutant dispersion studies.

768 **Acknowledgements** Elliott Lumet’s PhD thesis was funded by the Université Fédérale
769 Toulouse Midi-Pyrénées together with the Région Occitanie (ADI20, AtmoDrones project,
770 2020–2023). This work was granted access to the HPC resources of GENCI-TGCC/CINES
771 (A0062A10822 project, 2020–2022). The authors acknowledge Bastien Nony for prelimi-
772 nary code development and helpful discussion.

773 **Availability of data and codes** The dataset used in this paper is openly available
774 on a public repository (Lumet et al. 2024a). A notebook describing the construction and
775 validation of the POD–GPR surrogate model is openly available at [https://github.](https://github.com/eliott-lumet/pod_gpr_ppmls)
776 [com/eliott-lumet/pod_gpr_ppmls](https://github.com/eliott-lumet/pod_gpr_ppmls). Other analysis codes developed for this study are
777 available from the corresponding author upon reasonable request.

778 **Declaration of competing interests** The authors have no competing interests to
 779 declare that are relevant to the content of this article.

780 **Appendix: The nearest neighbor control surrogate model**

781 We use a Nearest Neighbor model (1-NN) as a simple baseline model against which we
 782 compare the POD-GPR accuracy. It is an appropriate control model because it represents
 783 the generalization error obtained by simply querying the available simulation dataset, and
 784 thus represents the minimum level of error that the POD-GPR must exceed to be worth
 785 using. The 1-NN is a classical k -Nearest Neighbor (k -NN) model (Hastie et al. 2009)
 786 with only one neighbor ($k = 1$). The 1-NN prediction is simply defined as the nearest
 787 LES field in the training dataset:

$$\mathbf{y}_{\text{surrogate}}(\boldsymbol{\theta}) = \mathbf{y}_{\text{LES}}^{\text{train}}(\boldsymbol{\theta}^*), \text{ with } \boldsymbol{\theta}^* = \min_{1 \leq i \leq N_{\text{train}}} d(\boldsymbol{\theta}_i^{\text{train}}, \boldsymbol{\theta}), \quad (19)$$

788 where d is the Euclidean distance in a rescaled input space:

$$d(\boldsymbol{\theta}^{(1)}, \boldsymbol{\theta}^{(2)}) = \sqrt{\left(\frac{\alpha_{\text{inlet}}^{(2)} - \alpha_{\text{inlet}}^{(1)}}{\alpha_{\text{inlet}}^{\text{max}} - \alpha_{\text{inlet}}^{\text{min}}}\right)^2 + \zeta^2 \left(\frac{u_*^{(2)} - u_*^{(1)}}{u_*^{\text{max}} - u_*^{\text{min}}}\right)^2} \quad (20)$$

789 where $\alpha_{\text{inlet}}^{\text{min}}$, $\alpha_{\text{inlet}}^{\text{max}}$, u_*^{min} , and u_*^{max} are the input space boundaries, and ζ is a rescaling
 790 factor that distorts the distances in the parameter space.

791 The hyperparameter ζ gives more or less weight to the friction velocity when searching
 792 for the closest LES field in the dataset (Eq. 19). It is optimized during training by
 793 cross-validation (Hastie et al. 2009) with 8-fold resampling of the train set. The best
 794 compromise between RMSE, VG and FMS(1 ppm) scores is obtained for $\zeta = 0.275$, which
 795 reduces the distances along the friction velocity axis and therefore gives more weight to
 796 the inlet wind direction parameter.

797 **References**

- 798 Antonioni, G., Burkhart, S., Burman, J., Dejoan, A., Fusco, A., Gaasbeek, R.,
799 Gjesdal, T., Jäppinen, A., Riikonen, K., Morra, P., Parmhed, O., and Santiago,
800 J. (2012). Comparison of CFD and operational dispersion models in an urban-
801 like environment. *Atmospheric Environment*, 47:365–372. ISSN 1352-2310. DOI:
802 10.1016/j.atmosenv.2011.10.053.
- 803 Bahlali, M. L., Dupont, E., and Carissimo, B. (2019). Atmospheric dispersion using
804 a Lagrangian stochastic approach: Application to an idealized urban area under neu-
805 tral and stable meteorological conditions. *Journal of Wind Engineering and Industrial*
806 *Aerodynamics*, 193:103976. ISSN 0167-6105. DOI: 10.1016/j.jweia.2019.103976.
- 807 Berkooz, G., Holmes, P., and Lumley, J. L. (1993). The proper orthogonal decomposition
808 in the analysis of turbulent flows. *Annual review of fluid mechanics*, 25(1):539–575.
809 DOI: 10.1146/annurev.fl.25.010193.002543.
- 810 Biltoft, C. (2001). Customer report for Mock Urban Setting Test. DPG Document
811 No. WDTC-FR-01-121, West Desert Test Center, U.S. Army Dugway Proving Ground,
812 Utah, USA.
- 813 Blocken, B., Stathopoulos, T., Saathoff, P., and Wang, X. (2008). Numerical evaluation
814 of pollutant dispersion in the built environment: Comparisons between models and
815 experiments. *Journal of Wind Engineering and Industrial Aerodynamics*, 96(10):1817–
816 1831. ISSN 0167-6105. DOI: 10.1016/j.jweia.2008.02.049. 4th International Symposium
817 on Computational Wind Engineering (CWE2006).
- 818 Blocken, B. (2014). 50 years of computational wind engineering: Past, present and
819 future. *Journal of Wind Engineering and Industrial Aerodynamics*, 129:69–102. ISSN
820 0167-6105. DOI: 10.1016/j.jweia.2014.03.008.
- 821 Blocken, B. (2015). Computational Fluid Dynamics for urban physics: Importance,
822 scales, possibilities, limitations and ten tips and tricks towards accurate and reli-

823 able simulations. *Building and Environment*, 91:219–245. ISSN 0360-1323. DOI:
824 10.1016/j.buildenv.2015.02.015. Fifty Year Anniversary for Building and Environment.

825 Braconnier, T., Ferrier, M., Jouhaud, J.-C., Montagnac, M., and Sagaut, P. (2011).
826 Towards an adaptive POD/SVD surrogate model for aeronautic design. *Computers &*
827 *Fluids*, 40(1):195–209. ISSN 0045-7930. DOI: 10.1016/j.compfluid.2010.09.002.

828 Brunton, S. L. and Kutz, J. N. (2019). *Data-Driven Science and Engineering: Ma-*
829 *chine Learning, Dynamical Systems, and Control*. Cambridge University Press. DOI:
830 10.1017/9781108380690.

831 Camelli, F., Lohner, R., and Hanna, S. (2005). VLES study of MUST experiment. In
832 *43rd AIAA Aerospace Sciences Meeting and Exhibit*. DOI: 10.2514/6.2005-1279.

833 Chang, J. and Hanna, S. (2004). Air quality model performance evaluation. *Meteorol.*
834 *Atm. Phys*, 87(1):167–196. DOI: 10.1007/s00703-003-0070-7.

835 Cheng, K., Lu, Z., Ling, C., and Zhou, S. (2020). Surrogate-assisted global sensitivity
836 analysis: an overview. *Structural and Multidisciplinary Optimization*, 61:1187–1213.
837 DOI: 10.1007/s00158-019-02413-5.

838 Chinesta, F., Ladeveze, P., and Cueto, E. (2011). A short review on model order reduction
839 based on proper generalized decomposition. *Archives of Computational Methods in*
840 *Engineering*, 18(4):395–404. ISSN 1886-1784. DOI: 10.1007/s11831-011-9064-7.

841 Cordier, L. and Bergmann, M. (2006). Réduction de dynamique par décomposition
842 orthogonale aux valeurs propres (POD) (in French). Lecture notes, Ecole
843 de printemps OCET. URL [https://www.math.u-bordeaux.fr/~mbergman/PDF/](https://www.math.u-bordeaux.fr/~mbergman/PDF/OuvrageSynthese/OCET06.pdf)
844 [OuvrageSynthese/OCET06.pdf](https://www.math.u-bordeaux.fr/~mbergman/PDF/OuvrageSynthese/OCET06.pdf). Accessed: 2023-12-01.

845 Dauxois, T., Peacock, T., Bauer, P., Caulfield, C. P., Cenedese, C., Górlé, C., Haller,
846 G., Ivey, G. N., Linden, P. F., Meiburg, E., Pinardi, N., Vriend, N. M., and Woods,
847 A. W. (2021). Confronting grand challenges in environmental fluid mechanics. *Phys.*
848 *Rev. Fluids*, 6:020501. DOI: 10.1103/PhysRevFluids.6.020501.

- 849 Defforge, C. L., Carissimo, B., Bocquet, M., Bresson, R., and Armand, P. (2021). Im-
850 proving numerical dispersion modelling in built environments with data assimilation
851 using the iterative ensemble Kalman smoother. *Boundary-Layer Meteorology*, 179(2):
852 209–240. ISSN 1573-1472. DOI: 10.1007/s10546-020-00588-9.
- 853 Defforge, C. L., Carissimo, B., Bocquet, M., Bresson, R., and Armand, P. (2019). Im-
854 proving CFD atmospheric simulations at local scale for wind resource assessment using
855 the iterative ensemble Kalman smoother. *Journal of Wind Engineering and Industrial*
856 *Aerodynamics*, 189:243–257. ISSN 0167-6105. DOI: 10.1016/j.jweia.2019.03.030.
- 857 Donnelly, R., Lyons, T., and Flassak, T. (2009). Evaluation of results of a numerical simu-
858 lation of dispersion in an idealised urban area for emergency response modelling. *Atmos.*
859 *Environ.*, 43(29):4416–4423. ISSN 1352-2310. DOI: 10.1016/j.atmosenv.2009.05.038.
- 860 EEA. (2020). Air quality in Europe. 2020 report, European Environment Agency. URL
861 <https://www.eea.europa.eu/publications/air-quality-in-europe-2020>.
- 862 Efthimiou, G. C., Bartzis, J. G., and Koutsourakis, N. (2011). Modelling concentra-
863 tion fluctuations and individual exposure in complex urban environments. *Journal of*
864 *Wind Engineering and Industrial Aerodynamics*, 99(4):349–356. ISSN 0167-6105. DOI:
865 10.1016/j.jweia.2010.12.007. The Fifth International Symposium on Computational
866 Wind Engineering.
- 867 El Garroussi, S., Ricci, S., De Lozzo, M., Goutal, N., and Lucor, D. (2020). As-
868 sessing uncertainties in flood forecasts using a mixture of generalized polynomial
869 chaos expansions. In *2020 TELEMAC-MASCARET User Conference*. URL <https://hal.science/hal-03444227/document>. Accessed: 2023-12-01.
- 871 Fellmann, N., Pasquier, M., Blanchet-Scalliet, C., Helbert, C., Spagnol, A., and Sinoquet,
872 D. (2023). Sensitivity analysis for sets : application to pollutant concentration maps.
- 873 Fernando, H. J. S., Lee, S. M., Anderson, J., Princevac, M., Pardyjak, E., and Grossman-
874 Clarke, S. (2001). Urban fluid mechanics: Air circulation and contaminant dispersion
875 in cities. *Environ. Fluid Mech.*, 1(1):107–164. DOI: 10.1023/A:1011504001479.

- 876 Forkman, J., Josse, J., and Piepho, H.-P. (2019). Hypothesis tests for principal compo-
877 nent analysis when variables are standardized. *Journal of Agricultural, Biological and*
878 *Environmental Statistics*, 24:289–308. DOI: 10.1007/s13253-019-00355-5.
- 879 Franke, J., Hellsten, A., Schlünzen, H., and Carissimo, B. (2007). Best practice guide-
880 line for the CFD simulation of flows in the urban environmen. Technical report,
881 COST European Cooperation in Science and Technology. URL [https://hal.science/](https://hal.science/hal-04181390)
882 [hal-04181390](https://hal.science/hal-04181390). Accessed: 2023-12-01.
- 883 García-Sánchez, C., van Beeck, J., and Górlé, C. (2018). Predictive large eddy simulations
884 for urban flows: Challenges and opportunities. *Building and Environment*, 139:146–156.
885 ISSN 0360-1323. DOI: 10.1016/j.buildenv.2018.05.007.
- 886 García-Sánchez, C., Philips, D., and Górlé, C. (2014). Quantifying inflow uncertainties for
887 CFD simulations of the flow in downtown Oklahoma City. *Building and Environment*,
888 78:118–129. ISSN 0360-1323. DOI: 10.1016/j.buildenv.2014.04.013.
- 889 García-Sánchez, C., Van Tendeloo, G., and Górlé, C. (2017). Quantifying inflow uncer-
890 tainties in RANS simulations of urban pollutant dispersion. *Atmospheric Environment*,
891 161:263–273. ISSN 1352-2310. DOI: 10.1016/j.atmosenv.2017.04.019.
- 892 Gicquel, L. Y., Gourdain, N., Boussuge, J.-F., Deniau, H., Staffelbach, G., Wolf, P.,
893 and Poinso, T. (2011). High performance parallel computing of flows in complex
894 geometries. *Comptes Rendus Mécanique*, 339(2):104–124. ISSN 1631-0721. DOI:
895 10.1016/j.crme.2010.11.006. High Performance Computing.
- 896 Górlé, C. and Iaccarino, G. (2013). A framework for epistemic uncertainty quantifica-
897 tion of turbulent scalar flux models for Reynolds-averaged Navier-Stokes simulations.
898 *Physics of Fluids*, 25(5):055105. ISSN 1070-6631. DOI: 10.1063/1.4807067.
- 899 Górlé, C., Garcia-Sanchez, C., and Iaccarino, G. (2015). Quantifying inflow and RANS
900 turbulence model form uncertainties for wind engineering flows. *Journal of Wind Engi-*
901 *neering and Industrial Aerodynamics*, 144:202–212. DOI: 10.1016/j.jweia.2015.03.025.

902 Gousseau, P., Blocken, B., Stathopoulos, T., and van Heijst, G. (2011). CFD simulation
903 of near-field pollutant dispersion on a high-resolution grid: A case study by LES and
904 RANS for a building group in downtown Montreal. *Atmos. Environ.*, 45(2):428–438.
905 ISSN 1352-2310. DOI: 10.1016/j.atmosenv.2010.09.065.

906 Gromke, C., Jamarkattel, N., and Ruck, B. (2016). Influence of roadside hedgerows on air
907 quality in urban street canyons. *Atmospheric Environment*, 139:75–86. ISSN 1352-2310.
908 DOI: 10.1016/j.atmosenv.2016.05.014.

909 Guo, M. and Hesthaven, J. S. (2018). Reduced order modeling for nonlinear structural
910 analysis using gaussian process regression. *Computer Methods in Applied Mechanics
911 and Engineering*, 341:807–826. ISSN 0045-7825. DOI: 10.1016/j.cma.2018.07.017.

912 Halton, J. H. (1964). Algorithm 247: Radical-inverse quasi-random point sequence.
913 *Communications of the ACM*, 7(12):701–702. DOI: 10.1145/355588.365104.

914 Hanna, S. R., Hansen, O. R., and Dharmavaram, S. (2004). FLACS CFD air quality model
915 performance evaluation with Kit Fox, MUST, Prairie Grass, and EMU observations.
916 *Atmos. Environ.*, 38(28):4675–4687. DOI: 10.1016/j.atmosenv.2004.05.041.

917 Hastie, T., Tibshirani, R., Friedman, J. H., and Friedman, J. H. (2009). *The elements of
918 statistical learning: data mining, inference, and prediction*, volume 2. Springer. DOI:
919 10.1007/978-0-387-21606-5.

920 Hsieh, K.-J., Lien, F.-S., and Yee, E. (2007). Numerical modeling of passive scalar
921 dispersion in an urban canopy layer. *Journal of Wind Engineering and Industrial
922 Aerodynamics*, 95(12):1611–1636. ISSN 0167-6105. DOI: 10.1016/j.jweia.2007.02.028.

923 Huang, C., Zhang, G., Yao, J., Wang, X., Calautit, J. K., Zhao, C., An, N., and Peng, X.
924 (2022). Accelerated environmental performance-driven urban design with generative
925 adversarial network. *Building and Environment*, 224:109575. ISSN 0360-1323. DOI:
926 10.1016/j.buildenv.2022.109575.

927 Kastner, P. and Dogan, T. (2023). A GAN-Based Surrogate Model for Instantaneous

928 Urban Wind Flow Prediction. *Building and Environment*, 242:110384. ISSN 0360-
929 1323. DOI: 10.1016/j.buildenv.2023.110384.

930 Kessy, A., Lewin, A., and Strimmer, K. (2018). Optimal whitening and decorrelation.
931 *The American Statistician*, 72(4):309–314. DOI: 10.1080/00031305.2016.1277159.

932 Klein, P., Leitl, B., and Schatzmann, M. (2007). Driving physical mechanisms of
933 flow and dispersion in urban canopies. *Int. J. Climatol.*, 27(14):1887–1907. DOI:
934 10.1002/joc.1581.

935 König, M. (2014). *Large-eddy simulation modelling for urban scale*. PhD thesis, Univer-
936 sity of Leipzig. URL [https://citeseerx.ist.psu.edu/document?repid=rep1&type=](https://citeseerx.ist.psu.edu/document?repid=rep1&type=pdf&doi=baab9d7b41623099c1b6d840c11821b8e31fac9b)
937 [pdf&doi=baab9d7b41623099c1b6d840c11821b8e31fac9b](https://citeseerx.ist.psu.edu/document?repid=rep1&type=pdf&doi=baab9d7b41623099c1b6d840c11821b8e31fac9b). Accessed: 2024-08-05.

938 Kraichnan, R. H. (1970). Diffusion by a random velocity field. *Phys. Fluids*, 13(1):22–31.
939 DOI: 10.1063/1.1692799.

940 Kumar, P., Feiz, A.-A., Ngae, P., Singh, S. K., and Issartel, J.-P. (2015). CFD simulation
941 of short-range plume dispersion from a point release in an urban like environment.
942 *Atmos. Environ.*, 122:645–656. DOI: 10.1016/j.atmosenv.2015.10.027.

943 Lamberti, G. and Gorlé, C. (2021). A multi-fidelity machine learning framework to predict
944 wind loads on buildings. *Journal of Wind Engineering and Industrial Aerodynamics*,
945 214:104647. ISSN 0167-6105. DOI: 10.1016/j.jweia.2021.104647.

946 Lassila, T., Manzoni, A., Quarteroni, A., and Rozza, G. (2014). Model order reduction
947 in fluid dynamics: challenges and perspectives. *Reduced Order Methods for modeling*
948 *and computational reduction*, pages 235–273. DOI: 10.1007/978-3-319-02090-7_9.

949 Lucas, D. D., Gowardhan, A., Cameron-Smith, P., and Baskett, R. L. (2016). Impact
950 of meteorological inflow uncertainty on tracer transport and source estimation in ur-
951 ban atmospheres. *Atmospheric Environment*, 143:120–132. ISSN 1352-2310. DOI:
952 10.1016/j.atmosenv.2016.08.019.

- 953 Lumet, E. (2024). *Assessing and reducing uncertainty in large-eddy simulation for mi-*
954 *cro-scale atmospheric dispersion*. PhD thesis, Université Toulouse III - Paul Sabatier.
955 URL <https://theses.fr/2024TLSES003>. Accessed: 2024-05-30.
- 956 Lumet, E., Jaravel, T., and Rochoux, M. C. (2024)a. PPMLES – Perturbed-Parameter
957 ensemble of MUST Large-Eddy Simulations. Dataset on Zenodo. To be published.
- 958 Lumet, E., Jaravel, T., Rochoux, M. C., Vermorel, O., and Lacroix, S. (2024)b. Assessing
959 the Internal Variability of Large-Eddy Simulations for Microscale Pollutant Dispersion
960 Prediction in an Idealized Urban Environment. *Boundary-Layer Meteorology*, 190(2):
961 9. ISSN 1573-1472. DOI: 10.1007/s10546-023-00853-7.
- 962 Manisalidis, I., Stavropoulou, E., Stavropoulos, A., and Bezirtzoglou, E. (2020). Envi-
963 ronmental and health impacts of air pollution: A review. *Frontiers in Public Health*, 8.
964 ISSN 2296-2565. DOI: 10.3389/fpubh.2020.00014.
- 965 Margheri, L. and Sagaut, P. (2016). A hybrid anchored-ANOVA – POD/Kriging method
966 for uncertainty quantification in unsteady high-fidelity CFD simulations. *Journal of*
967 *Computational Physics*, 324:137–173. ISSN 0021-9991. DOI: 10.1016/j.jcp.2016.07.036.
- 968 Marrel, A., Perot, N., and Mottet, C. (2015). Development of a surrogate model and
969 sensitivity analysis for spatio-temporal numerical simulators. *Stochastic Environmental*
970 *Research and Risk Assessment*, 29(3):959–974. ISSN 1436-3259. DOI: 10.1007/s00477-
971 014-0927-y.
- 972 Masoumi-Verki, S., Haghghat, F., and Eicker, U. (2022). A review of advances to-
973 wards efficient reduced-order models (ROM) for predicting urban airflow and pol-
974 lutant dispersion. *Building and Environment*, 216:108966. ISSN 0360-1323. DOI:
975 10.1016/j.buildenv.2022.108966.
- 976 Mendil, M., Leirens, S., Armand, P., and Duchenne, C. (2022). Hazardous atmo-
977 spheric dispersion in urban areas: A Deep Learning approach for emergency pollution
978 forecast. *Environmental Modelling & Software*, 152:105387. ISSN 1364-8152. DOI:
979 10.1016/j.envsoft.2022.105387.

- 980 Milliez, M. and Carissimo, B. (2007). Numerical simulations of pollutant dispersion
981 in an idealized urban area, for different meteorological conditions. *Boundary-Layer*
982 *Meteorology*, 122(2):321–342. DOI: 10.1007/s10546-006-9110-4.
- 983 Miyagusuku, R., Yamashita, A., and Asama, H. (2015). Gaussian processes with input-
984 dependent noise variance for wireless signal strength-based localization. In *2015 IEEE*
985 *International Symposium on Safety, Security, and Rescue Robotics (SSRR)*, pages 1–6.
986 DOI: 10.1109/SSRR.2015.7442993.
- 987 Mons, V., Margheri, L., Chassaing, J.-C., and Sagaut, P. (2017). Data assimilation-
988 based reconstruction of urban pollutant release characteristics. *Journal of Wind*
989 *Engineering and Industrial Aerodynamics*, 169:232–250. ISSN 0167-6105. DOI:
990 10.1016/j.jweia.2017.07.007.
- 991 Montazeri, H. and Blocken, B. (2013). CFD simulation of wind-induced pressure coef-
992 ficients on buildings with and without balconies: Validation and sensitivity analysis.
993 *Build Environ.*, 60:137–149. ISSN 0360-1323. DOI: 10.1016/j.buildenv.2012.11.012.
- 994 Murata, T., Fukami, K., and Fukagata, K. (2020). Nonlinear mode decomposition with
995 convolutional neural networks for fluid dynamics. *Journal of Fluid Mechanics*, 882:A13.
996 DOI: 10.1017/jfm.2019.822.
- 997 Nagel, T., Schoetter, R., Masson, V., Lac, C., and Carissimo, B. (2022). Numerical
998 analysis of the atmospheric boundary-layer turbulence influence on microscale transport
999 of pollutant in an idealized urban environment. *Boundary-Layer Meteorology*, 184(1):
1000 113–141. DOI: 10.1007/s10546-022-00697-7.
- 1001 Neophytou, M., Gowardhan, A., and Brown, M. (2011). An inter-comparison of
1002 three urban wind models using Oklahoma City Joint Urban 2003 wind field measure-
1003 ments. *Journal of Wind Engineering and Industrial Aerodynamics*, 99(4):357–368. DOI:
1004 10.1016/j.jweia.2011.01.010.
- 1005 Nicoud, F. and Ducros, F. (1999). Subgrid-scale stress modelling based on the

1006 square of the velocity gradient tensor. *Flow Turbul. Combust.*, 62(3):183–200. DOI:
1007 10.1023/A:1009995426001.

1008 Nony, B. X., Rochoux, M. C., Jaravel, T., and Lucor, D. (2023). Reduced-order modeling
1009 for parameterized large-eddy simulations of atmospheric pollutant dispersion. *Stoch.*
1010 *Environ. Res. Risk Assess.*, 37(6):2117–2144. ISSN 1436-3259. DOI: 10.1007/s00477-
1011 023-02383-7.

1012 Nony, B. X. (2023). *Reduced-order models under uncertainties for microscale atmospheric*
1013 *pollutant dispersion in urban areas: exploring learning algorithms for high-fidelity model*
1014 *emulation*. Phd thesis, Université de Toulouse, France.

1015 Pasquier, M., Jay, S., Jacob, J., and Sagaut, P. (2023). A Lattice-Boltzmann-
1016 based modelling chain for traffic-related atmospheric pollutant dispersion at the lo-
1017 cal urban scale. *Building and Environment*, 242:110562. ISSN 0360-1323. DOI:
1018 10.1016/j.buildenv.2023.110562.

1019 Picheny, V., Ginsbourger, D., Roustant, O., Haftka, R. T., and Kim, N.-H. (2010).
1020 Adaptive designs of experiments for accurate approximation of a target region. *Journal*
1021 *of Mechanical Design*, 132(7):071008. ISSN 1050-0472. DOI: 10.1115/1.4001873.

1022 Politis, D. N. and Romano, J. P. (1994). The stationary bootstrap. *J. Am. Stat. Assoc.*,
1023 89(428):1303–1313. DOI: 10.1080/01621459.1994.10476870.

1024 Ramshaw, J., O’Rourke, P., and Amsden, A. (1986). Acoustic damping for explicit
1025 calculations of fluid flow at low Mach number. Technical report no. LA-10641-MS,
1026 Los Alamos National Laboratories, USA. URL [https://inis.iaea.org/collection/
1027 NCLCollectionStore/_Public/17/074/17074782.pdf](https://inis.iaea.org/collection/NCLCollectionStore/_Public/17/074/17074782.pdf). Accessed: 2023-12-01.

1028 Rasmussen, C. E., Williams, C. K., et al. (2006). *Gaussian processes for machine learning*,
1029 volume 1. Springer. DOI: 10.7551/mitpress/3206.001.0001.

1030 Santiago, J. L., Dejoan, A., Martilli, A., Martin, F., and Pinelli, A. (2010). Comparison
1031 between large-eddy simulation and Reynolds-Averaged Navier–Stokes computations for

1032 the MUST field experiment. Part I: Study of the flow for an incident wind directed
1033 perpendicularly to the front array of containers. *Boundary-Layer Meteorology*, 135(1):
1034 109–132. DOI: 10.1007/s10546-010-9466-3.

1035 Schatzmann, M. and Leitl, B. (2011). Issues with validation of urban flow and dispersion
1036 CFD models. *J. Wind Eng. Ind. Aerodyn.*, 99(4):169–186. ISSN 0167-6105. DOI:
1037 10.1016/j.jweia.2011.01.005. The Fifth International Symposium on Computational
1038 Wind Engineering.

1039 Schatzmann, M., Olesen, H., and Franke, J. (2010). COST 732 model evalua-
1040 tion case studies: approach and results. Technical report, University of Ham-
1041 burg, Meteorological Institute. URL [https://www.researchgate.net/profile/
1042 George-Efthimiou-3/post/Has-fluent-been-compared-to-starccm/attachment/
1043 59d6585379197b80779ae4bd/AS%3A538043318628353%401505290931380/download/
1044 5th_Docu_May_10.pdf](https://www.researchgate.net/profile/George-Efthimiou-3/post/Has-fluent-been-compared-to-starccm/attachment/59d6585379197b80779ae4bd/AS%3A538043318628353%401505290931380/download/5th_Docu_May_10.pdf). Accessed: 2023-12-01.

1045 Schmidt, O. T. and Colonius, T. (2020). Guide to spectral proper orthogonal decompo-
1046 sition. *AIAA journal*, 58(3):1023–1033. DOI: 10.2514/1.J058809.

1047 Schönfeld, T. and Rudgyard, M. (1999). Steady and unsteady flow simulations using the
1048 hybrid flow solver AVBP. *AIAA journal*, 37(11):1378–1385. DOI: 10.2514/2.636.

1049 Sirovich, L. (1987). Turbulence and the dynamics of coherent structures. I. Coherent struc-
1050 tures. *Quarterly of applied mathematics*, 45(3):561–571. DOI: 10.1090/qam/910462.

1051 Smirnov, A., Shi, S., and Celik, I. (2001). Random flow generation technique for large
1052 eddy simulations and particle-dynamics modeling. *J. Fluids Eng.*, 123(2):359–371. ISSN
1053 0098-2202. DOI: 10.1115/1.1369598.

1054 Sousa, J. and Górlé, C. (2019). Computational urban flow predictions with Bayesian
1055 inference: Validation with field data. *Building and Environment*, 154:13–22. ISSN
1056 0360-1323. DOI: 10.1016/j.buildenv.2019.02.028.

1057 Sousa, J., García-Sánchez, C., and Górlé, C. (2018). Improving urban flow predictions

1058 through data assimilation. *Building and Environment*, 132:282–290. ISSN 0360-1323.
1059 DOI: 10.1016/j.buildenv.2018.01.032.

1060 Spicer, T. O. and Tickle, G. (2021). Simplified source description for atmospheric disper-
1061 sion model comparison of the Jack Rabbit II chlorine field experiments. *Atmospheric*
1062 *Environment*, 244:117866. ISSN 1352-2310. DOI: 10.1016/j.atmosenv.2020.117866.

1063 Stein, M. L. (1999). *Interpolation of spatial data: some theory for kriging*. Springer Series
1064 in Statistics. Springer Science & Business Media. DOI: 10.1007/978-1-4612-1494-6.

1065 Taira, K., Brunton, S. L., Dawson, S. T. M., Rowley, C. W., Colonius, T., McKeon, B. J.,
1066 Schmidt, O. T., Gordeyev, S., Theofilis, V., and Ukeiley, L. S. (2017). Modal analysis of
1067 fluid flows: An overview. *AIAA Journal*, 55(12):4013–4041. DOI: 10.2514/1.J056060.

1068 Tominaga, Y. and Stathopoulos, T. (2007). Turbulent Schmidt numbers for CFD analysis
1069 with various types of flowfield. *Atmospheric Environment*, 41(37):8091–8099. ISSN
1070 1352-2310. DOI: 10.1016/j.atmosenv.2007.06.054.

1071 Tominaga, Y. and Stathopoulos, T. (2009). Numerical simulation of dispersion around an
1072 isolated cubic building: Comparison of various types of $k-\epsilon$ models. *Atmospheric En-*
1073 *vironment*, 43(20):3200–3210. ISSN 1352-2310. DOI: 10.1016/j.atmosenv.2009.03.038.

1074 Tominaga, Y., Wang, L. L., Zhai, Z. J., and Stathopoulos, T. (2023). Accuracy of CFD
1075 simulations in urban aerodynamics and microclimate: Progress and challenges. *Building*
1076 *and Environment*, 243:110723. ISSN 0360-1323. DOI: 10.1016/j.buildenv.2023.110723.

1077 Vasaturo, R., Kalkman, I., Blocken, B., and van Wesemael, P. (2018). Large eddy
1078 simulation of the neutral atmospheric boundary layer: Performance evaluation of three
1079 inflow methods for terrains with different roughness. *J. Wind Eng. Ind. Aerodyn.*, 173:
1080 241–261. DOI: 10.1016/j.jweia.2017.11.025.

1081 Vinuesa, R. and Brunton, S. L. (2022). Enhancing computational fluid dynamics with
1082 machine learning. *Nature Computational Science*, 2(6):358–366. ISSN 2662-8457. DOI:
1083 10.1038/s43588-022-00264-7.

- 1084 Weerasuriya, A., Zhang, X., Lu, B., Tse, K., and Liu, C. (2021). A gaussian process-
1085 based emulator for modeling pedestrian-level wind field. *Building and Environment*,
1086 188:107500. ISSN 0360-1323. DOI: 10.1016/j.buildenv.2020.107500.
- 1087 Winiarek, V., Bocquet, M., Saunier, O., and Mathieu, A. (2012). Estimation of errors
1088 in the inverse modeling of accidental release of atmospheric pollutant: Application to
1089 the reconstruction of the cesium-137 and iodine-131 source terms from the Fukushima
1090 Daiichi power plant. *Journal of Geophysical Research: Atmospheres*, 117(D5). DOI:
1091 10.1029/2011JD016932.
- 1092 Wise, D., Boppana, V., Li, K., and Poh, H. (2018). Effects of minor changes in the mean
1093 inlet wind direction on urban flow simulations. *Sustain. Cities Soc.*, 37:492–500. ISSN
1094 2210-6707. DOI: 10.1016/j.scs.2017.11.041.
- 1095 Wu, Y. and Quan, S. J. (2024). A review of surrogate-assisted design optimization for
1096 improving urban wind environment. *Building and Environment*, 253:111157. ISSN
1097 0360-1323. DOI: 10.1016/j.buildenv.2023.111157.
- 1098 Wu, Y., Zhan, Q., Quan, S. J., Fan, Y., and Yang, Y. (2021). A surrogate-assisted
1099 optimization framework for microclimate-sensitive urban design practice. *Building and*
1100 *Environment*, 195:107661. ISSN 0360-1323. DOI: 10.1016/j.buildenv.2021.107661.
- 1101 Xiang, S., Fu, X., Zhou, J., Wang, Y., Zhang, Y., Hu, X., Xu, J., Liu, H., Liu, J., Ma, J.,
1102 and Tao, S. (2021). Non-intrusive reduced order model of urban airflow with dynamic
1103 boundary conditions. *Building and Environment*, 187:107397. ISSN 0360-1323. DOI:
1104 10.1016/j.buildenv.2020.107397.
- 1105 Xiao, D., Heaney, C., Fang, F., Mottet, L., Hu, R., Bistrrian, D., Aristodemou, E.,
1106 Navon, I., and Pain, C. (2019). A domain decomposition non-intrusive reduced or-
1107 der model for turbulent flows. *Computers & Fluids*, 182:15–27. ISSN 0045-7930. DOI:
1108 10.1016/j.compfluid.2019.02.012.
- 1109 Xiao, H., Wu, J.-L., Wang, J.-X., Sun, R., and Roy, C. (2016). Quantifying and re-
1110 ducing model-form uncertainties in Reynolds-averaged Navier–Stokes simulations: A

- 1111 data-driven, physics-informed Bayesian approach. *Journal of Computational Physics*,
1112 324:115–136. ISSN 0021-9991. DOI: 10.1016/j.jcp.2016.07.038.
- 1113 Yee, E. and Biltoft, C. A. (2004). Concentration fluctuation measurements in a plume
1114 dispersing through a regular array of obstacles. *Boundary-Layer Meteorology*, 111(3):
1115 363–415. DOI: 10.1023/B:BOUN.0000016496.83909.ee.
- 1116 Yue Yang, G.-W. H. and Wang, L.-P. (2008). Effects of subgrid-scale modeling on
1117 lagrangian statistics in large-eddy simulation. *Journal of Turbulence*, 9:N8. DOI:
1118 10.1080/14685240801905360.